UNIVERSIDADE
BEIRA INTERIOR

Fatigue crack propagation study on the Portuguese Air Force Epsilon TB-30 aircraft

Versão final após apresentação

Beatriz Carolina Vasco Gonçalves da Costa Fernandes

Dissertação para a obtenção do Grau de Mestre em
Engenharia Aeronáutica
(Mestrado integrado)

Orientador: Professor Doutor Pedro Gamboa
Coorientador: Tenente Tomás Barros

Novembro 2021

Dedicatory

À minha família.

Acknowledgements

Antes de mais, gostaria de agradecer à Força Aérea Portuguesa pelo oportunidade que me foi dada para contribuir para o projecto SHM TB-30, que é de grande importância. Gostaria também de agradecer ao Major-General José Lourenço da Saude que foi quem permitiu o desenvolvimento deste trabalho com esta entidade.

Gostaria também de expressar a minha enorme gratidão ao Tomás que, para além de propor o tema desta dissertação, provou ser um mentor exemplar, tendo fornecido orientação e apoio ao longo de todo o processo com dedicação e rigor. A sua contribuição foi crucial para o desenvolvimento deste estudo e, sem ele, não teria sido possível.

Gostaria de agradecer ao Professor Doutor Pedro Gamboa pelos seus conselhos, orientação, interesse e a pronta ajuda que prestou ao longo de todo o desenvolvimento deste trabalho.

Cumpre-me também agradecer à pessoa que foi um dos grandes pilares e que permitiu que esta dissertação fosse realizada sem nunca me deixar desanimar, o maior obrigado ao João porque sem ele nada disto teria sido possível.

Aos meus amigos e à Covilhã com quem tive o prazer de passar dos melhores anos da minha vida, um bem haja.

Por último, mas certamente não menos importante, agradeço à minha família pelo apoio incondicional que sempre me deram, pela compreensão, preocupação e amor, que sempre estiveram presentes. A minha mais profunda gratidão.

Resumo

A fadiga é um fenómeno causado por cargas dinâmicas que se caracteriza pela propagação de fissuras e pode culminar na rotura total de um material. No sector aeronáutico militar, particularmente na formação de pilotos, este problema assume especial importância dada a diversidade de missões e manobras que são levadas a cabo. O avião Epsilon TB-30 é utilizado na Força Aérea Portuguesa para instrução básica de pilotagem na Frota 101, na Base Aérea nº11 em Beja. No âmbito da monitorização da integridade estrutural, uma aeronave da frota foi recentemente instrumentada com um sistema que inclui a instalação de um acelerómetro no centro de gravidade da aeronave e cinco extensómetros em locais críticos da aeronave, o que levou à definição dos principais objectivos deste trabalho: o desenvolvimento de uma ferramenta de propagação automática de fenda para um local crítico na estrutura da aeronave, bem como a comparação na propagação de uma fenda quando sujeita a um regime de voo severo e não-severo, voos típicos na operacção da frota Epsilon.

A fim de simular a propagação da fenda, este trabalho incluiu um modelo de elementos finitos desenvolvido no software Ansys para a obtenção dos valores do factor de intensidade de tensão para vários tamanhos de fenda. Foi também realizado, com o recurso a Matlab, a modelação da propagação da fenda utilizando as leis de propagação Walker e NASGRO para a obtenção de uma expressão para o factor geométrico, Y. Posteriormente, foi realizada uma análise comparativa do comportamento de crescimento da fenda para diferentes regimes de severidade de voo, leis de propagação e tamanhos iniciais da fenda.

Finalmente, foi desenvolvida uma aplicação web que permite simular de forma simples e automática a propagação da fenda para um voo real.

Palavras-chave

Propagação de fenda, Fator de intensidade de tensão, Fator geométrico, Leis de propagação, Ansys, Regimes de voo.

Abstract

Fatigue is a phenomenon caused by dynamic loads which is characterised by the propagation of cracks and can culminate in the complete fracture of a material. In the military aeronautical sector, particularly in pilot training, this problem takes on special importance given the diversity of missions and manoeuvres that are carried out. The Epsilon TB-30 aircraft is used in the Portuguese Air Force for basic piloting instruction in the 101st Fleet, at the Air Base 11 in Beja. Within the scope of Structural Integrity monitoring, a fleet aircraft was recently instrumented with a system that includes the installation of an accelerometer at the aircraft's centre of gravity and five strain gauges in critical locations of the aircraft, ,which led to the definition of the main objectives of this work: the development of an automatic crack propagation tool for a critical location in the aircraft structure, as well as the comparison of the crack growth rate when subjected to a severe and non-severe flight regime, typical flights in the operation of the Epsilon fleet.

In order to simulate the crack propagation, this work included a finite element model developed in Ansys software to obtain the stress intensity factor values for several crack sizes. It was also carried out, with the resource to Matlab, the crack propagation modeling using the Walker and NASGRO propagation laws to get an expression for the geometric factor Y. Subsequently, a comparison analysis of crack growth behaviour for different flight severity regimes, propagation laws and initial crack sizes was conducted.

Finally, a web application was developed to straightforwardly and automatically simulate the crack propagation for a real-world flight.

Keywords

Crack propagation, Stress intensity factor, Geometric factor, Propagation laws, Ansys, Flight regimes.

Contents

List of Figures

List of Tables

Acrónimos

AFA Academia da Força Aérea

CAD Computer Aided Design

CAE Computer Aided Engineering

CEAT Centre d'Essais Aeronautique de Toulouse

CG Centre of Gravity

DOF Degrees Of Freedom

FAP Portuguese Air Force

FCG Fatigue Crack Growth

FE Finite Element

FEM Finite Element Method

FH Flight Hours

LEFM Linear Elastic Fracture Mechanics

MSR Modular Signal Recorder

SHM Structural Health Monitoring

SIF Stress Intensity Factor

Nomenclature

The next list describes several symbols that will be later used within the body of the document

$A_0,\ A_1,\ A_2 and\ A_3$ NASGRO model coefficients

$n_P,\ n_W,\ n_N$ Exponents for the laws of Paris, Walker and NASGRO respectively

$p,\ q$ Exponents of NASGRO's law

U Elastic energy of the material

u Displacement vector in the x direction

x Coordinate along the wing

α Material constraint factor

ΔK Variation of the stress intensity factor

ΔK_{eff} Effective variation of K with crack closing

ΔK_{th} Limit of non-propagation

$\Delta\sigma$ Stress variation over one cycle

ε Extension

Γ Arbitrary contour surrounding the crack

γ Walker law load ratio control parameter

ν Poisson's coefficient

$\overline{\Delta K}$ Walker model parameter

σ Nominal stress

σ_a Stress amplitude

σ_m Mean stress in a load cycle

$\sigma_x, \sigma_y, \sigma_z$ Axial components of stress.

σ_y Yield stress

σ_{max} Maximum stress in a load cycle

σ_{min} Minimum stress in a load cycle

σ_{uts} Tensile strength

$\tau_{xy}, \tau_{xz}, \tau_{yz}$ Shear stress components

θ Angle in front of the crack

a Crack depth

A_k NASGRO model parameter

B_k NASGRO model parameter

$c_0,\ c_2$ Geometric constants

C_P, C_W, C_N Coefficients for Paris, Walker and NASGRO, respectively

C_{th} Initiation Coefficient

D Drag

E Young's Modulus

F Work exerted by a force

f Newman crack closing function

F_s Boundary correction

f_w Finite width correction factor

f_θ Angular function

G Energy parameter

g Fine-tuning curve-fitting function

H_S bending multiplier

i Iteration index

J J Integral

j Angular index

K Stress Intensity Factor

K_C Fracture toughness

K_{crit} K Critical value

K_{IC} Fracture toughness for mode I

K_{max} Maximum stress intensity factor

K_{min} Minimum stress intensity factor

K_{op} Opening stress intensity

L Lift

L_0 Lift on the root of the wing

$L_d(x)$ Lift distribution on the wing

L_t Lift generated by horizontal stabilizer

L_w Lift generated by the wings

n Number of cycles performed

n_f Number of cycles to failure

n_i Number of cycles leading to crack initiation

n_p Number of cycles to catastrophic failure, final rupture

N_z	Load factor
Q	Shape factor for elliptical stress
R	Ratio between minimum and maximum stress
r_p	Radius of the plastic zone
S_b	Remote bending stress
S_t	Remote uniform tension stress
S_{max}	Maximum applied stress
T	Thrust
t	Thickness
t_0	Thickness reference
W	Deformation energy density of the material
W_a	Weight of the aircraft
Y	Geometric Factor
r_p	Size of the plastic deformation zone

Chapter 1

Introduction

1.1 Context

The Epsilon TB-30 aircraft manufactured by Daher and acquired by the Portuguese Air Force in 1989 is operated by Squadron 101 at the Air Base Nº11 in Beja, for basic and elementary pilot instruction. It is a two-seat tandem aircraft with a low and short wing and retractable landing gear. The six-cylinder horizontal engine is of automatic injection and has a feeding and lubrication device that allows inverted flight and drives a propeller of constant speed. The configuration of its instrument panel, its cruising speed, the robustness of its airframe, which supports from +6.7G to -3.35G, and the sensitivity of its controls, give it characteristics similar to those of a small conventional fighter aircraft [1], Figure 1.1.

Figure 1.1: Portuguese Air Force Epsilon TB-30 Aircraft

Table 1.1: Aircraft Parameters

Dimensions				
Wingspan	Wing Area	Aspect Ratio	Height	Length
7.92m	$9m^2$	7	2.66m	7.59m
Performance				
Maximum speed	Cruising speed	Maximum range	Maximum autonomy	Service ceiling
520 km/h	370 km/h	680 NM	03h45	24.000 ft

At the design stage of the aircraft, the manufacturer Daher based its maintenance program on full-scale fatigue tests performed at the Centre d'Essais Aeronautique de Toulouse (CEAT) [2]. From these tests, among other conclusions, the manufacturer found that the life limit of the aircraft is controlled by the behaviour of the most critical location of the aircraft structure, which is at the frame cross-member, depicted in Figure 1.2 (a) and (b), which is the component of the fuselage where the main spar of both wings connects. Considering the operation of the aircraft in missions with high load factors, it is fundamental to understand if the operation assumptions considered by the manufacturer, when defining its maintenance

plan, are applicable to the *Portuguese Air Force*, taking into account the operation regime performed. Therefore, in order to review and update the most adequate maintenance plan, it becomes necessary to provide fatigue life information so that it becomes possible to change the maintenance program in use.

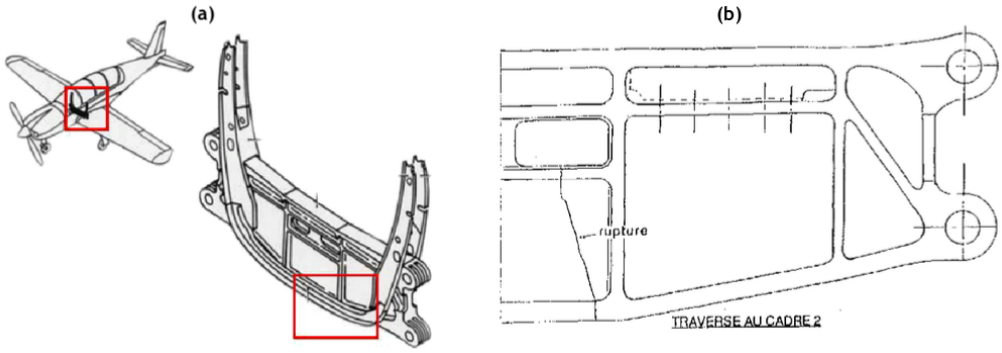

Figure 1.2: (a) Detail of the frame area on the aircraft, Milharadas [3] (b) Frame crack detected by CEAT [2]

Through the aircraft's instrumentation, consisting of the installation and integration of five strain gauges, an accelerometer, and a Data Acquisition Unit (DAU), at critical locations on the aircraft such as the spar and frame, it is possible to collect and store extension data and the load factor to which it is subjected during the operating cycle. This allows fatigue life information to be obtained, thereby allowing monitoring the fleet operation and the validation of the analytical and computational models developed in the design phase. The data obtained also allows an assessment of the severity of operation to which the fleet is subjected through comparison with the results of full scale fatigue tests.

Numerous studies have been carried out as part of the TB-30 SHM project, with the aim of implementing a Structural Health Monitoring (SHM) system on the Epsilon TB-30 fleet. In 2003, Silva [4] proceeded to the instrumentation of one of the aircraft, with 70 hours of flight time being monitored, allowing to obtain values of acceleration at the centre of gravity (CG) of the aircraft and stresses in the main spar. This was followed in 2004 by Milharadas [3] work where a representative specimen of the crossbeam of frame C2 was designed and a crack propagation study was carried out, where it was concluded that the operation spectrum of the *Portuguese Air Force* (FAP) fleet was more severe than the reference spectrum considered by the manufacturer. In 2009, Serrano [5] performed a crack propagation study and a calculation of the accumulated damage with the data obtained from Silva's instrumentation, also concluding that the operation performed by FAP is more severe than the one considered by the manufacturer.

In 2017, due to the need to obtain data representative of the FAP operation regime, the Epsilon TB-30 fleet was instrumented with the MSR 165 equipment that allows to monitor the aircraft acceleration during operation. At the time, Gameiro [6] carried out a study to calculate the accumulated damage and concluded that FAP's operational regime had a lower severity than that recommended by the manufacturer. This instrumentation allowed, between June 2017 and May 2019, to obtain acceleration data in the aircraft's vertical axis for a time span of 1161.31 flight hours , characterising the fleet's operating regime. In the same year, a software was implemented for flight data processing, cycle counting and obtaining the accumulated load spectrum of the FAP fleet.

In more recent studies, in 2018, Martins [7] performed a numerical analysis of crack propagation in the transom of frame C2, concluding that FAP's operation is more severe than the reference operation. In 2019, with FAP's need to provide the manufacturer with flight data characteristic of the fleet operation, Barros [8] carried out the instrumentation of an aircraft by installing an accelerometer in its CG and five strain gauges in critical locations where data of 1000 Flight Hours (FH) of operation was collected . He

also verified that the FAP fleet presents a more severe operating regime than the reference regime.

1.2 Objectives

Following these studies, and continuing within the scope of the SHM TB-30 project, this project arose from FAP's need to monitor the crack propagation in a location previously considered critical in the structure of the Epsilon TB-30 aircraft.

The main objective of this work is to provide FAP with a tool to predict the crack size evolution in a critical aircraft location through the development of an application where it is possible to insert flight data, select the propagation model, initial crack size and points around it, being thus possible to simulate the crack growth for several flight regimes, from aerobatic flights to more stable regimes.

To support this characterization, the following intermediate objectives were established:

- Develop a tool to predict automatic crack propagation using the Finite Element Method.
- Model one of the critical components of the aircraft using finite elements and estimate the propagation based on the loads measured by the SHM-TB30 system.
- Validate the developed application through a flight data processing.
- Compare the crack growth for 2 different flight regimes, severe and non-severe.

1.3 Work Structure

This work is composed of 5 chapters. Chapter 2 is a literature review on the concept of fatigue, its historical evolution, causes and consequences. It is also given an explanation about fracture mechanics, more specifically about linear elastic fracture mechanics (LEFM), as well as concepts that define its formalism. It is also introduced the phenomenon of fracture propagation and the finite element method applied to LEFM.

In chapter 3, the main focus is to obtain the geometric factor, Y, for the Epsilon airframe. To do so, a simple cubic structure was initially modeled in order to validate the values of K (stress intensity factor) obtained in Ansys software and comparing them with tabulated values. It was then proceeded to the modelling of the aircraft structure in question and to the insertion of a semi- elliptical crack of various sizes at the critical location of the geometry. With the values of K taken from this software, and resorting to Matlab, the expression of Y was obtained.

In chapter 4, the development of an automatic crack propagation tool was conducted. In the first part of this chapter it is given an introduction of its functioning, an explanation of the possible inputs to select and a detailed explanation of the crack propagation algorithm. In the second part of the chapter is provided a description and comparison of the different flight severity regimes in the Portuguese Air Force Epsilon fleet operation. Then, several simulations were performed in order to study the behavior of the crack for several different scenarios, using real flight data from the aircraft instrumentation.

Finally, Chapter 5 draws the final conclusions of this work, presenting the main results as well as the limitations that restrict the validity of the study and also possible future research directions to be developed.

Chapter 2

State of the art

Material fatigue refers to changes in properties resulting from the application of cyclic loads [9]. The field of fracture mechanics, as it is known today, was practically nonexistent before World War II [10]. It was believed that fractures were an insignificant phenomena and that they would never become real threats to large structures such as ships and aircrafts. However, during the war, a large number of catastrophic failures apparently occurred without explainable causes. Ship structures were welded to save time in assembling due to the great demand for provisions that crossed the Atlantic Ocean. The effects of temperature, stress concentrations and residual stresses were not well understood. Due to this metallurgical ignorance of the weld and materials, the *Liberty* series ships are, until today, a classic example of accidents caused by fatigue fractures. Many of them suffered such fractures on the high seas that they sank before completing the crossing of the Atlantic. It was observed that the material lost the ductility necessary to resist low temperatures. Since then, countless scientists and engineers have made pioneering contributions to a better understanding of this phenomenon

In 1829 a German mining worker, W.A.J. Albert, studied and reported the failure of mine elevation cables resulting from cyclical loads, this is the first known record on metal fatigue. Albert showed that the application of cyclic loads would cause failures with loads of less than expected intensity [11].

The use of ferrous materials has increased considerably over the years, particularly in railways and bridges. This increase led to the number of accidents and victims reaching unknown levels. It is estimated that, in Britain, between the 1860s and 1870s, they lost their lives on railway lines as a result of derailments caused by fractures of wheels, axles and rails, about 200 people. The first detailed study of metal fatigue took place in 1842, after a tragic railway accident near Versailles, France, in which the cause of this accident was attributed to fatigue failure originating in the locomotive's front axle [12] .

Between 1852 and 1869, in Germany, A. Wöhler conducted systematic studies on fatigue failures at full scale, created an experimental rotary flex fatigue machine and was able to determine the range of stress for which the life of the rail steel he was testing would be "infinite".[13] His work also led to the characterization of fatigue behavior in terms of stress versus number of cycles (S-N) curves, still known today as Wöhler curves, thus introducing the concept of fatigue resistance limit stress.

In the second half of the 19th century, in 1864, Fairbarn concluded that, when subjected to cyclical stresses, iron beams would rupture with only a third of the maximum force to be applied. In 1874, H. Gerber, and Goodman, in 1899, developed methods for calculating fatigue with the aim of introducing it into a project, as well as formulation proposals to modulate the effect of medium stress. In 1886, Bauschinger demonstrated that the elastic limit of metals subject to reversible loads could be different from that observed in the deformation in 2 constant cycles and also confirmed many of the results reported by Wöhler. By the end of this century, about 80 articles had already been published in different areas of application and, in 1910, Basquin proposed the first mathematical equation to represent the S-N curves.

Griffith appears, in 1921, with one of the first contributions to the study of Fracture Mechanics. He developed a failure criterion and related fatigue to crack growth[9]. Many other notable contributions

from this period include names such as: Bairstow (1910), Moore & Seeley (1915), Ludwik (1919), Masing (1926) and Soderberg (1939).

Years later, specifically in 1954, Coffin and Manson reformulated Basquin's equation with the intention of characterizing fatigue based on deformations. Palmgren, in 1924, and later Miner, in 1945, carried out investigations in the modeling of fatigue damage accumulation. Langer, in 1937, carried out the first work in the area of fatigue with shipments of variable amplitude.

In the postwar period, in 1956, G.R.Irwin concluded that the basic tools needed to study fractures were already available. His first major contribution was to extend Griffith's approach to metals. Irwin demonstrated that the stress state in front of the failure could be expressed in terms of the scalar quantity known as the stress intensity factor, K. With the arrival of the new approach to linear elastic fracture mechanics (LEFM), attempts were made to characterize the growth of fatigue cracks in terms of stress intensity [13]
.

That same year, Wells used fracture mechanics to demonstrate that the catastrophic failures suffered in the fuselage of several jet aircraft *The Comet*, of the company Havilland Aircraft, in England, resulted from fatigue failures that would have reached their critical size. These fractures started in the windows and were caused by insufficient local reinforcement, combined with the square corners of the windows where a high stress concentration was produced. Since then, aircraft windows have taken oval or round geometric shapes in order to decentralize stresses and, consequently, metallic fatigue. [9][10]

The Second World War separates two distinct epochs in the history of fracture mechanics, but there is some ambiguity as to how the period between the end of the war and the present should be divided. A possible historical frontier occurred around 1960, when the fundamentals of the elastic linear fracture mechanics were well established, and the researchers redirected their attention to plasticity in front of failure. [10]

In 1961, Paris, Gomez and Anderson were the first to suggest that the increase in fracture advance per stress cycle, da/dN, could be related to the stress intensity factor (SIF) ΔK, during stress cycles with constant load. [10] Linear Elastic Fracture mechanics (LEFM) is no longer valid when there is significant plastic deformation in front of the crack.Between 1960 and 1961, researchers, including Irwin, Dugdale , Barenblatt and Wells, developed analyses to correct the yielding at the front of the crack. In 1969, Rice developed a parameter to characterize the nonlinear behavior of the material before the fracture occurred. He managed to generalize the energy release rate for non-linear materials and showed that this rate could be expressed as a line integral called J Integral [9].

The field of fracture mechanics underwent construction in the last decades of the 20th century. With the massification of sectors such as the automobile, naval and aeronautics, scientific progress in this area became imperative, as well as the application of more sophisticated models in fatigue analysis. The continuous explosion of computational technology has made it possible to generate entirely new areas in the research of fracture mechanics [9].

2.1 Concept of fatigue

Fatigue is a process of localized damage to a material, caused by cyclical loads, where there is a reduction in the load capacity of structural components. This reduction leads to a slow rupture of the material due to the microscopic advance of the crack at each loading cycle [14]. The number of cycles to failure, n_f, is given by Equation 2.1 where n_i represents the number of cycles leading to the initiation of the crack and n_p, the number of cycles for the propagation of the crack until the component is completely broken.

$$n_f = n_i + n_p \quad (2.1)$$

During these loads, in places of greatest tension, plastic deformations may occur. These deformations lead to a deterioration of the material, inducing permanent damage and giving rise to the beginning of a crack. As the component undergoes an increasing number of load cycles, the length of the crack increases, eventually causing it to break completely. According to several authors, including Young-lee Li [14] and Branco [15]. The fatigue process involves 4 main steps: (1) crack nucleation, (2) microscopic crack growth, (3) crack propagation and finally (4) final rupture. This process is represented in Figure 2.1.

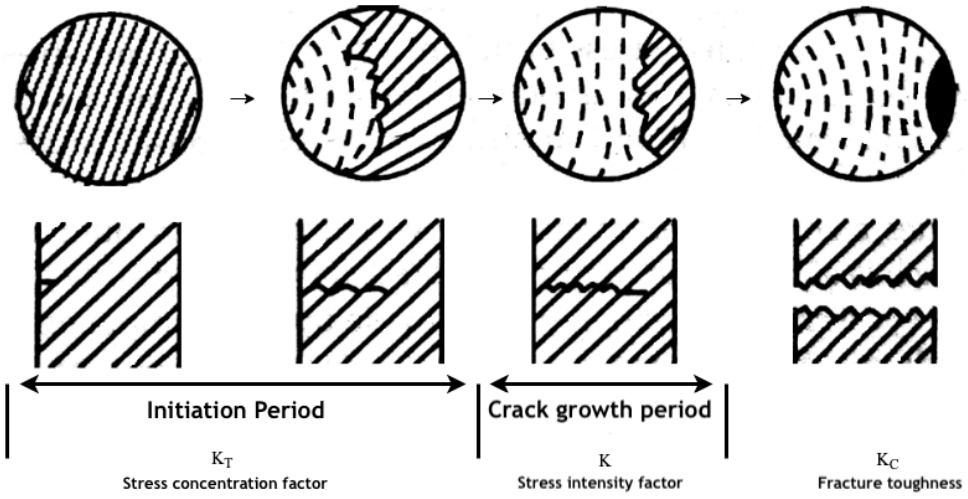

Figure 2.1: Fatigue process steps [16]

The conditions for the nucleation of micro defects and for the growth of the crack are strongly influenced by discontinuities, porosities or inclusions. The cracks in the material tend to be originated in a cutting plane or close to areas conducive to the concentration of stresses. This cutting plane usually occurs on the surface or at the grain boundaries of the material. The surface is more prone to nucleation of fatigue cracks due to the fact that the plastic deformation of the crystalline grains found there is more accessible than those located inside. This occurs as a result to the fact that the surface grains are less constrained to deformation, because they find the free surface of the structure, being able to deform without meeting resistance. The crack nucleation phase, due to fatigue, depends on the cyclic shear stresses that act, while for the crack propagation phase, it is the tensile stresses that lead to the gradual growth of micro cracks until the final rupture.

Bearing in mind that the mechanisms that act on nucleation and propagation are different, it is necessary to use different criteria to evaluate a failure due to fatigue in the nucleation and in the propagation phase. The fatigue life can be divided into two phases: initiation period and a crack growth period, as can be seen in Figure 2.1. The nucleation and microscopic growth of the crack represent the first phase, where the propagation of the crack occurs in the order of two grains in the plane of shear stress. At this stage, the plasticity of the crack front is severely affected by the sliding characteristics, grain size, orientation and tension level. This is due to the fact that the crack size is comparable to the material's microstructure [15].

The crack growth period covers its macroscopic growth before rupture. The crack propagation in this phase is normal to the plane of tensile stress and in the direction of local maximum shear stress. In this period, the characteristics of the crack are less affected by the properties of the microstructure than in the first phase. This is because the plastic area in front of the crack is already much larger than the material's microstructure.

At this stage, there are three ways to propagate the crack: by coalescence of microcavities, by microcleavage and by ductile striation. However, the latter mechanism should be highlighted, because due to the successive positions of the front of the crack, the fracture surface will present streaks. These striations represent thousands or even millions of load cycles and point to the point of origin of the crack propagation. The proportion between the propagation phase and the final break indicates the degree of overload to which the component was subjected. As soon as the crack reaches a certain dimension, the entire system becomes unstable and the remaining section of the component can no longer support the applied load, leading to the final break [14].

2.2 General aspects of fatigue

The typical forms of cyclic loads that the components are subjected to are random in nature and vary in magnitude over their useful life. These loads can have a constant or varying with time range with time as shown in Figure 2.2 [14].

Cyclic loads where the amplitude and the average stress remain constant, are defined by 5 parameters that characterize the load represented in Figure 2.2 (a). These parameters are: stress amplitude σ_a, average stress σ_m, maximum stress σ_{max}, minimum stress σ_{min} and by R, which represents the ratio between the minimum and maximum stress. However, it is possible to fully define the cyclic load with only two of the referred parameters [17].

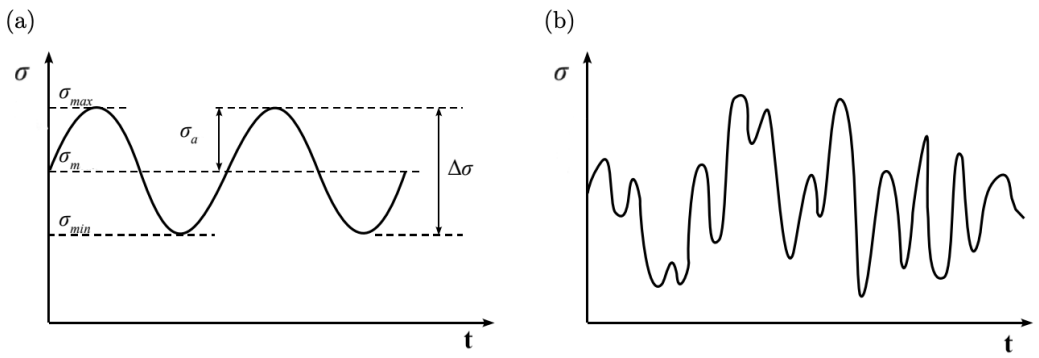

Figure 2.2: Cyclic loads of constant amplitude (a) and random amplitude (b)

The stress range, $\Delta\sigma$, is the difference between the maximum and minimum stress values. The average of the maximum and minimum values gives the average stress, σ_m. Half of the stress range is called the stress amplitude, σ_a, which is the variation over the mean. The mathematical expressions for these basic definitions are given by the expressions 2.2 and 2.3.

$$\sigma_a = \frac{\Delta\sigma}{2} = \frac{\sigma_{max} - \sigma_{min}}{2}, \quad (2.2) \qquad \sigma_m = \frac{\sigma_{max} + \sigma_{min}}{2} \quad (2.3)$$

In turn, the maximum stress, σ_{max}, and the minimum stress, σ_{min}, can be expressed, respectively by:

$$\sigma_{max} = \sigma_m + \sigma_a, \quad (2.4) \qquad \sigma_{min} = \sigma_m - \sigma_a \quad (2.5)$$

The average stress can also be characterized in terms of the stress ratio, R, that is an important parameter and is defined by the algebraic ratio of the minimum and maximum cyclic stresses given by Equation2.6. It is widely used to distinguish different conditions of cyclic loads of constant amplitude in fatigue analysis. Another less used parameter, in the fatigue load, is the algebraic ratio of the stress amplitude in relation to the average stress, called A, given by Equation 2.7.

$$R = \frac{\sigma_{min}}{\sigma_{max}}, \quad (2.6) \qquad A = \frac{\sigma_a}{\sigma_m} \quad (2.7)$$

The case of a sinusoidal load cycle is called alternating or fully reversible with a stress ratio of $R = -1$. In this case, the maximum and minimum cyclic stresses are equal, (σ_m=0). Loads with null ratio, $R = 0$, are called pulsating, (σ_m=σ_{max}/2).

Random loading is complex and can contain any combination of cyclical stresses and unlike the growth of a fatigue crack in constant amplitude, its propagation in variable amplitude does not depend only on the current load ΔR and R, being provided by the time course of the load. This phenomenon is attributed to the sequence effect. Due to this fact, loads of variable amplitude can lead to accelerated or delayed growth of the crack and consequently affect the service life, linked or prolonged. Random loads that involve more than one amplitude and average stress represent, in a more realistic way, what a structure is submitted to.

A real example of variable load sequences is the case of an aircraft flight. Each mission profile can be divided into different phases: taxiing and take-off phase, ascent, cruise phase, aerobatics, descent and landing. The load spectrum for each phase is dependent on a number of variables. For example, the magnitude of the load at which a wing is encountered during ascents and descents depends on its speed, weight and burst factor. Figure 2.3 shows the load environment to which a FAP Epsilon TB-30 aircraft is subjected during a flight [17].

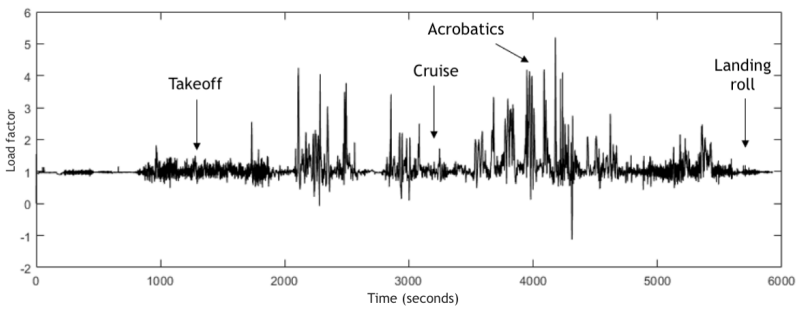

Figure 2.3: Time evolution of the load factor on a flight of the Epsilon TB-30 aircraft

2.3 Linear Elastic Fracture Mechanics

One of the properties of solid materials is their ability to resist or transmit stresses. The response to these efforts is closely related to the material's ability to be able to deform elastically or plastically. In this sense, LEFM is based on the assumption of a generalized linear elastic behavior of the solid.

The LEFM takes into account the effect of the tension in front of the crack and assumes, as an approximation, the crack as being perfectly elastic, with theoretically infinite stresses in front of the crack. This theory is based on an analytical procedure that relates the magnitude and distribution of the stress field in front of the crack, with the nominal stress applied to the solid, crack length and geometry, in order to define the conditions for which the crack propagates. This field can be described in terms of K, stress intensity factor and the similar to Material Mechanics , it assumes that the material in question is homogeneous, isotropic, continuous and that the stresses are proportional to the deformations. The LEFM is implemented in the analysis of low-ductile materials, that is, in which there is no considerable plastic deformation, before fracture.

2.3.1 Fracture modes in front of the crack

In general, a material can suffer loads from any direction in relation to the crack. The stress fields and displacement modes in front of the crack can be classified into modes, I, II and III, represented in Figure 2.4 [12].

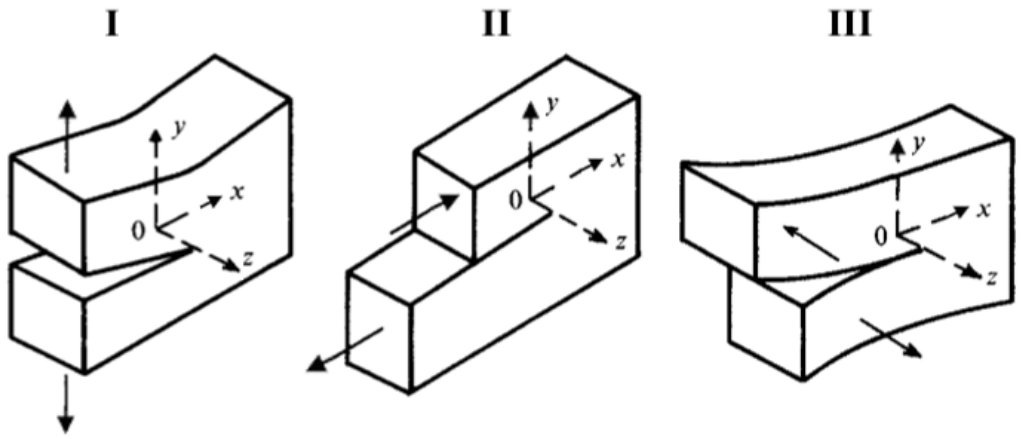

Figure 2.4: Breaking modes in front of the crack [9]

Mode I (opening mode), is characterized by being the most severe due to the displacement of the two crack surfaces, moving away from each other directly. In this case, the applied load and displacement are perpendicular to the crack surfaces. Mode II (sliding mode) occurs when the two cracked faces are moved, sliding over each other. The applied direction and load are parallel to the crack plane. Mode III (tearing mode), is characterized by the application of a load parallel to the plane and in front of the crack. The displacements of the crack walls, in this case, are anti-symmetrical in relation to the x-y and x-z planes.

Despite the existence of mixed loads, when there is a combination of the different propagation modes mentioned, mode I represents the most frequent type of separation in the life of a structure, in which the

propagation direction of the crack is always perpendicular to the direction of the applied load. Being the most common in practical engineering applications and consequently the most studied mode, it presents a greater development in analytical and experimental methods compared to other modes [17] [9].

2.3.2 Stress intensity factor

The concept of stress intensity factor K, introduced at the beginning of this chapter in general terms, fully characterizes the conditions at the crack front in an elastic and isotropic linear material. Figure 2.5 shows a coordinate system that describes the stresses in the areas close to the crack. The polar coordinates r and θ are in the x-y plane, which is normal to the crack plane.

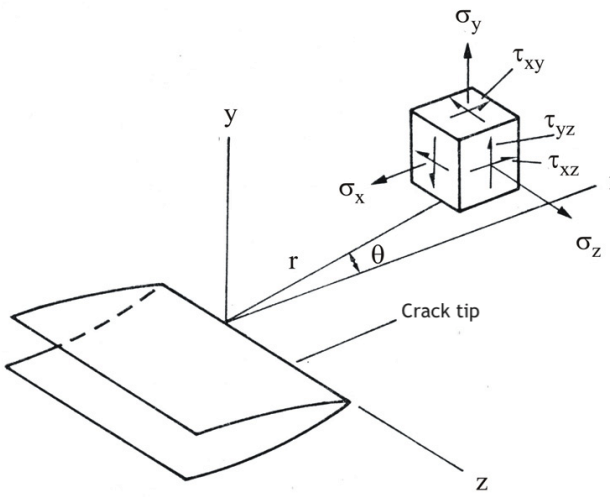

Figure 2.5: Stresses in front of the crack [18]

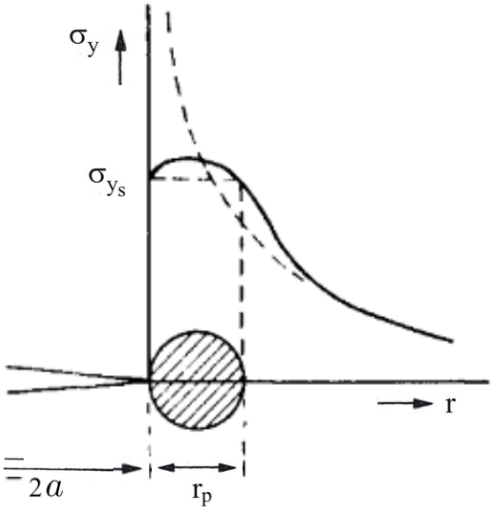

Figure 2.6: Approximate distribution of stress in front of the crack, including plastic zone [12]

For mode I loads, the state of the stresses at the crack front can be described by the set of Equations above in which, σ_x, σ_y and σ_z correspond to the axial stress components, τ_{xy},τ_{xz} and τ_{yz} represent the shear stress components and θ refers to the angle in front of the crack. Analyzing the set of equations, it is possible to state that this linear elastic stress analysis presents a singularity, since it predicts that the non-zero stresses tend to an infinite value at the end of the crack, when the parameter r tends to 0, due to the fact that these stresses are proportional to the inverse of $\sqrt{r}$, which represents a physical impossibility, see Figure 2.6.

In real materials, these stresses are limited by the localized flow that occurs in a region in front of the crack, called the plastic zone. The effects that this zone causes are shown in figure 2.6. The LEFM principles are valid as long as the size of this plastic zone is reduced, when compared to the overall dimensions of the crack and the solid, that is, when r_p is small in relation to a, being r_p the radius of the plastic zone.

$$\sigma_x = \frac{K_I}{\sqrt{2\pi r}} cos(\frac{\theta}{2})[1 - sin(\frac{\theta}{2})sin(\frac{3\theta}{2})] \quad (2.8)$$

$$\sigma_y = \frac{K_I}{\sqrt{2\pi r}} \cos(\frac{\theta}{2})[1 + \sin(\frac{\theta}{2})\sin(\frac{3\theta}{2})] \quad (2.9)$$

$$\tau_{xy} = \frac{K_I}{\sqrt{2\pi r}} \cos(\frac{\theta}{2})\sin(\frac{\theta}{2})\cos(\frac{3\theta}{2}) \quad (2.10)$$

$$\sigma_z = 0 \quad \text{(Plane stress)} \quad (2.11)$$

$$\sigma_z = \nu(\sigma_{xx} - \sigma_{yy}) \quad \text{(Plane strain)} \quad (2.12)$$

$$\tau_{xz} = 0 = \tau_{yz} \quad (2.13)$$

It is also possible to state that the stresses in the vicinity of the crack front are proportional to the K_I parameter and the remaining factors depend only on the coordinates r and θ. . In this way, the magnitude of the stress field in front of the crack can be characterized by assigning a value to the K_I, factor, which is an indicator of the severity of the crack. For this loading mode, mode I, the stress intensity factor can be calculated according to the expression 2.14, where Y is the geometric factor, a is the crack size and σ is the nominal stress value [19].

$$K_I = Y\sigma\sqrt{\pi a} \quad (2.14)$$

2.3.3 Fracture toughness

Since the stress intensity factor, K, characterizes the stress distribution in front of the crack, it is assumed that, from a critical value, the crack resistance limit is exceeded. This value is defined as K_{IC}, called fracture toughness. This critical value is a property of the material and depends on characteristics such as load rate, temperature and stress state in front of the crack. The failure criterion in this case is given by Equation 2.15:

$$K_I \geq K_{IC} \quad (2.15)$$

Fracture toughness can then be defined as the ability of a material to resist cracking without suffering a total rupture. Ductile materials under normal load rates have the ability to absorb more energy and plastically deform before breaking, thus having higher fracture toughness. Fragile materials, on the other hand, suffer, instantly breaking under low stresses, presenting low fracture toughness. It is important to note that the load capacity or residual strength of a structure is significantly affected by the presence of cracks and is substantially less than the strength of a structure undamaged [17]. This parameter is dependent on the thickness of the material and defines three distinct regions called: plane state of stresses, transition behavior and plane state of strain [15]. These regions can be seen in Figure 2.7.

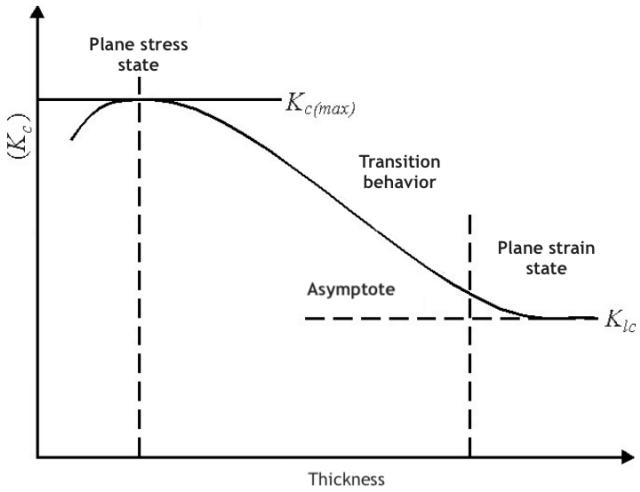

Figure 2.7: Stress state at the crack front for plane stress and plane strain [20] (adapted)

As the thickness of the material decreases, the restriction to the plastic flow decreases and the plane stress state is reached. When the thickness reaches a certain dimension, when the size of the plastic area of the crack's slot is in the order of the thickness of the material, the value of fracture toughness reaches a maximum value, $K_{C(max)}$. As the thickness increases, the size of the plastic zone decreases and therefore the toughness gradually decreases until it is reached a plateau. The apparent asymptote observed in the graph is represented by K_{IC}, used to denote fracture toughness under the condition of plane strain. The K_{IC} measurement standards were established by the American Society for Testing and Materials (ASTM). In the plane strain state, toughness behaves independently of the increase in thickness [10] [21].

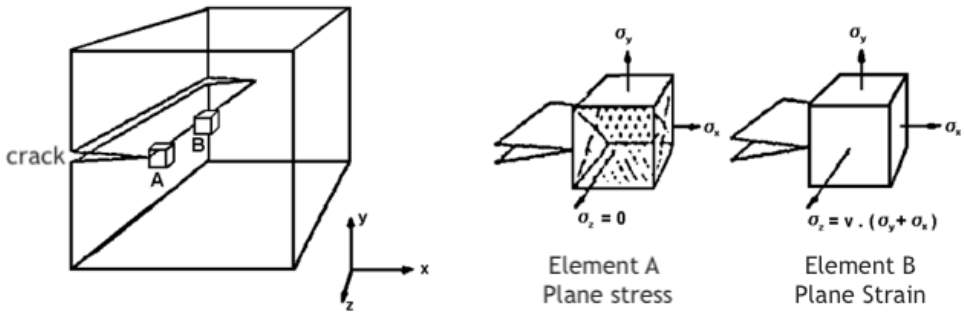

Figure 2.8: Crack front rupture modes [22] (adapted)

For thick components, that is, in a plane strain state and considering mode I of loading, the fracture surface is typically flat and normal to the direction of load application. In this state, it would be expected that the material found in the plastic zone would flow freely and that there would be deformation in the direction of the thickness. However, the surrounding material, of an elastic nature, is unable to keep up with this contraction and a phenomenon of plastic contraction is observed, at the same time a triaxial state of tension is established.

The plane stress state is characterized by the absence of tension perpendicular to the component surface σ_z. These two conditions are outlined in Figure 2.8, where a specimen with a moderate thickness is represented, containing a crack where they are two cubes, A and B are positioned. These cubes are positioned close to the surface and in the center of the specimen, respectively. A consequence of these two conditions is the way in which the material presents deformation, since the plane of maximum shear stress varies. This difference causes fracture in 45° planes with the load application axis, when in a plane stress state, and normal to the load application axis ,when in a state of plane strain. It is verified, therefore, that the energy necessary to produce fracture in the plane stress state is higher, since a large part is used in the deformation of the material.

2.3.4 Energy considerations

Griffith invoked the first law of thermodynamics to formulate a fracture theory based on a simple energy balance. According to this theory, a crack becomes unstable and, therefore, fracture occurs, when the change in deformation energy resulting in an increase in crack growth, is sufficient to overcome the surface energy of the material. Griffith was the first to propose the energy criterion for fracturing fragile materials, such as glass. He suggested that the rupture occurs when the energy release rate, resulting from the propagation of a crack, is greater than a critical value of the G_C [10].

However, it is Irwin who is primarily responsible for developing the current version of this approach: the rate of energy release G, which is defined as the rate of change in energy (W) with the crack area, for a material linear elastic. For a crack of length $2a$ in an infinite plate subjected to an applied stress, the energy release rate is given by the expression 2.16:

$$G = \frac{d(F-U)}{dA} = \frac{dW}{dA} = \frac{\pi\sigma^2 a}{E} \quad (2.16)$$

Where F represents the work done by an external force, U is the elastic energy contained in the material, E is Young's modulus and σ is the applied stress. Later Irwin proposed extending Griffith's approach to metals and used the stress intensity factor, K, to characterize fracture conditions. Irwin related the stress intensity factor to the energy release rate, two parameters that describe the behavior of cracks. While G describes the global behavior, K is a local parameter [10] [12]. For linear elastic materials, under loading mode I, K and G are listed as follows:

For plane stress:

$$G = \frac{K^2}{E} \quad (2.17)$$

for plane strain:

$$G = \left(1-\nu^2\right)\frac{K^2}{E} \quad (2.18)$$

2.3.5 Integral J

The LEFM is only valid as long as the non-linear deformation of a material is confined to a small dimension surrounding the crack. Since it is virtually impossible to characterize the fracture behavior in many materials with the LEFM, an alternative model of fracture mechanics was needed. In this segment, Rice introduces the concept of J Integral.

The J integral contour has had great success as a fracture characterization parameter for non-linear materials. By idealizing elastic-plastic deformation as a nonlinear elastic, Rice provided the basis for extending the methodology of fracture mechanics far beyond the limits of LEFM validity [23]. The expression of the energy release rate for an elastic two-dimensional case can be expressed as:

$$J = \int_{\Gamma} W dy - T \cdot \frac{\partial u}{\partial x} ds \quad (2.19)$$

Where Γ represents an arbitrary contour surrounding the crack, as can be seen in Figure 2.9, u is the displacement vector, y is the distance along the normal direction to the crack plane, s is the arc length along the contour, T is the tensile vector at the contour points and W is the deformation energy density of the material. This last parameter is defined by:

$$W = \int_0^{\varepsilon_{ij}} \sigma_{ij} d\varepsilon_{ij} \quad (2.20)$$

Where σ_{ij} and ε_{ij} are the stress and strain tensors, respectively. The components in the traction vector are:

$$T_i = \sigma_{ij} n_j \quad (2.21)$$

Where n_J are the unit components of the normal vector to Γ.

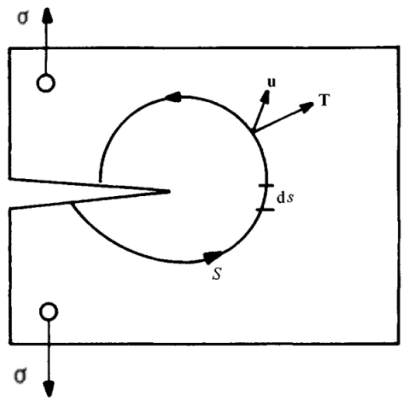

Figure 2.9: Arbitrary contour around the crack front [9]

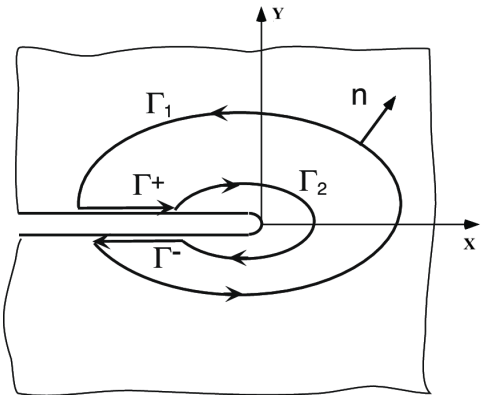

Figure 2.10: Independence of integral contour[24]

Rice demonstrated that the value of the integral J is independent of the integration path in front of the crack, thus assuming the same value for any contour of the crack, as shown in Figure 2.10. Additionally,

the parameter G and the J are related, since they represent the same amount, rate of change of potential energy in relation to to the crack advance [9]. However, these two parameters are applied to different regimes: while J can be applied to both linear and non-linear materials, G can only be applied in the LEFM regime. It should be noted, then, through the relation 2.22, that for linear elastic solids:

$$J = G = \frac{dW}{dA} \quad (2.22)$$

2.4 Crack propagation

The fracture mechanics aims to estimate the number of cycles that lead to a crack with initial length a_i, reaching its final length a_f. As mentioned in section 2.3.2, K is an essential parameter in addressing the crack's growth behavior, as long as it is in an elastic situation and the plastic deformation is limited to a small region in the crack front [17]. A fatigue loading introduces a cyclic stress in the crack front that varies between K_{max} and K_{min}, the interval between these two extremes is given by ΔK, as expressed below:

$$\begin{aligned} \Delta K &= K_{max} - K_{min} \\ &= Y\sigma_{max}\sqrt{\pi a} - Y\sigma_{min}\sqrt{\pi a} \\ &= Y\Delta\sigma\sqrt{\pi a} \end{aligned} \quad (2.23)$$

In general, results obtained experimentally show that a crack propagates slowly with each loading cycle and that the crack growth will increase as the amplitude of the loading increases [15]. This loading amplitude can be related to the stress ratio, R, and this parameter also applies to the corresponding K values as expressed in 2.24:

$$R = \frac{\sigma_{min}}{\sigma_{max}} = \frac{K_{min}}{K_{max}} \quad (2.24)$$

The crack propagation study can be done through the relationship between the crack growth rate of da/dn, the variation of the stress intensity factor ΔK and the stress ratio R, expressed in 2.25 . For each crack length, a, ΔK can be calculated by equation 2.23 and the results can be expressed in da/dn vs. ΔK curves [25].

$$\frac{da}{dn} = f\left(\Delta K, R\right) \quad (2.25)$$

In order to find a model that best fits the set of experimental data, several crack propagation laws were formulated, in order to represent the evolution of cracks as a function of the number of cycles. Throughout this section a more refined analysis of some of these models is made, exploring their characteristics in detail and their domains of validity.

2.4.1 Paris Law

The first relation obtained that describes the behavior of da/dn and ΔK was formulated by Paris, having been determined experimentally. This relationship of empirical origin is given by Equation2.26

$$\frac{da}{dn} = C_p \Delta K^{n_p} \quad (2.26)$$

In this equation C_p and n_p are material properties and n_p represents the slope in the bi-logarithmic scale curve, specifically in region II of Figure 2.11 (a). The sigmoidal curve represented contains three distinct regions: I, II and III. Phase I of the curve is characterized by discontinuous growth mechanisms and the existence of a propagation threshold ΔK_{th}, below which the applied loads do not cause damage to the cracked part and the crack does not propagate. The propagation of cracks in this area is controlled by the microstructure of the material, medium tension, frequency and environmental conditions.

The propagation region II corresponds to the stable crack propagation zone and is characterized by an exponential relationship between da/dn and ΔK, this region is described by the Paris law. The crack propagation rate in this area is influenced by environmental conditions, however, it is less influenced by the average tension and the microstructure.

Region III includes the highest ΔK range, at this stage there is an unstable crack propagation where the growth rate increases rapidly leading eventually to the final rupture [15] [10].

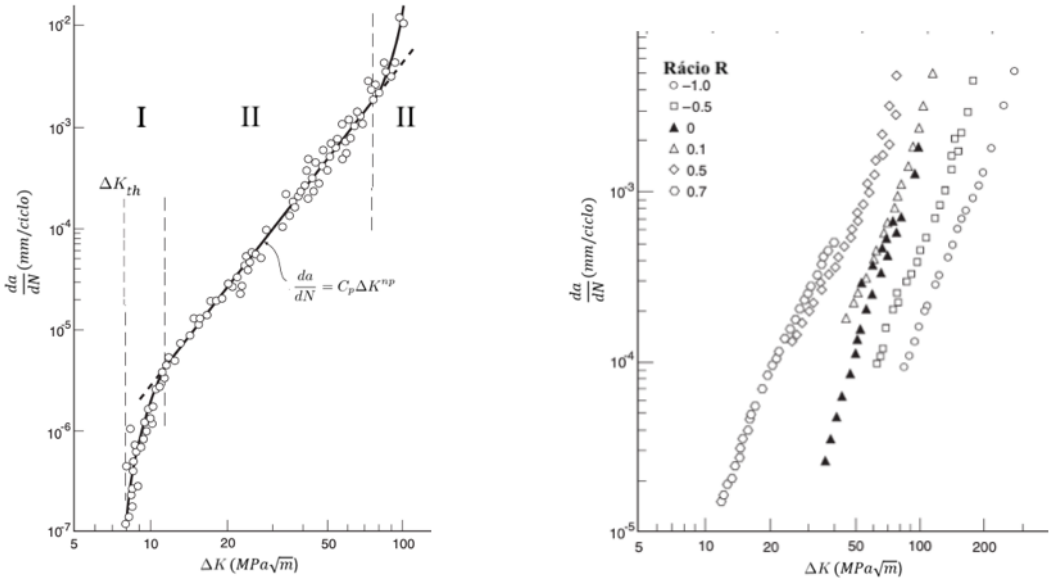

Figure 2.11: (a) Experimental data on the growth rate of a fatigue crack [19] (b) Influence of R on the crack growth rate in experimental data [19]

However, the Paris law does not accurately reflect the da/dn and ΔK relation since it does not apply to regions I and III where the crack growth is slow or fast. Using Equation 2.26 to model regions I and III can result in a life estimate that does not reflect reality. In addition, this equation does not take into account the effects of the stress ratio. By varying this parameter, as shown in figure2.11 (b), it is possible to observe distinct curves for each R value, with an increase in the growth rate of the da/dn crack [17]

2.4.2 Walker's Law

Another attempt to provide an empirical relationship to describe the crack growth data was made by Walker. The crack growth rate equation proposed is similar to the Paris relationship, but takes into account the effect of the stress ratio R in region II [14]. He proposed a parameter ranging from zero to the maximum SIF, (K_{max}) for R=0, expressed in Equation 2.27.

$$\overline{\Delta K} = K_{max}\,(1-R)^{\gamma} \quad (2.27)$$

Where γ is a constant proposed by Walker to assess the effect of R on the crack growth rate. According to Dowling [19], this constant can vary between 0.3 and 1, so the above equation can be rewritten as:

$$\overline{\Delta K} = \Delta K\,(1-R)^{\gamma-1} = \frac{\Delta K}{(1-R)^{1-\gamma}} \quad (2.28)$$

Substituting $\overline{\Delta K}$ for ΔK K in the Paris equation (2.26), the expression relative to Walker Law is obtained:

$$\frac{da}{dn} = C_W\left(\overline{\Delta K}\right)^{n_W} = C_W\left(\frac{\Delta K}{(1-R)^{1-\gamma}}\right)^{n_W} \quad (2.29)$$

In the expression above, n_W and C_w are constant and represent in a bi logarithmic reference, respectively, the slope and the ordinate at the origin. The following graphs represented in the figure 2.12 show the crack growth rates, in an example material, for various stress ratios R and for various values of γ: 0.3, 0.5 (typical value for metals) and 0.9 respectively.

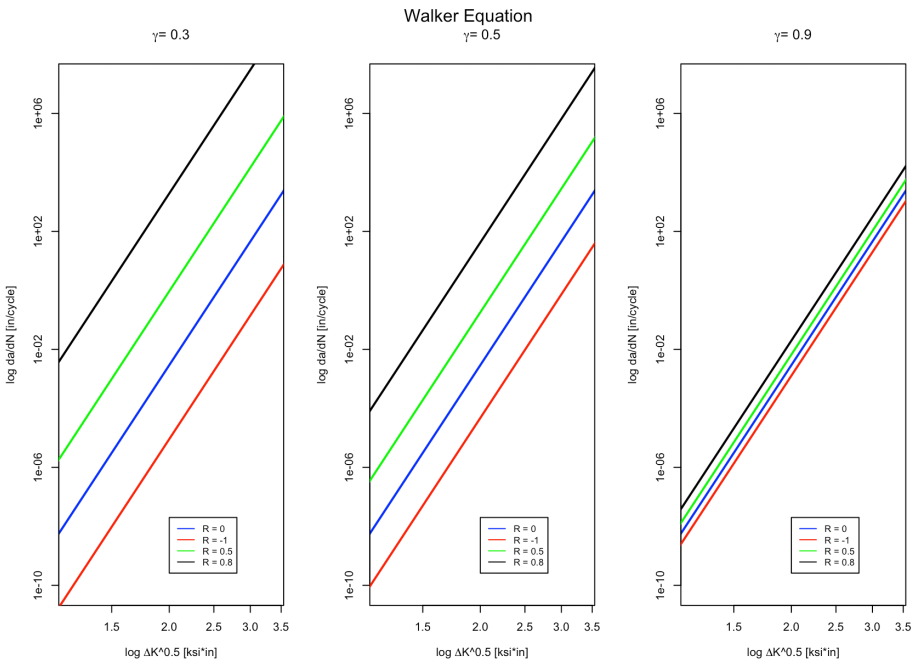

Figure 2.12: Walker equation for several values of γ [20] (adapted)

It is possible to observe that for low values of γ, the value of R causes a great impact on the growth rate of the crack, on the contrary, with the increase of γ the effect of R is attenuated. When γ takes the value of 0.9, in the third graph, the stress ratio ceases to have any effect on the crack growth rate. When $\gamma = 1$, simply, $\overline{\Delta K} = \Delta K$ is obtained, from equation 2.27. It is important to note that the value of γ, for a material may depend on whether the stress ratio is positive or negative. When R takes a negative value it means that there is a compressive load in the cycle.

For fragile materials, it appears that the compressive load does not significantly contribute to the growth of the crack, the value of γ for these materials presents values close to zero, resulting in a delay in the rate of da/dN. Therefore, for $R < 0$ and with $\gamma = 0$, $\overline{\Delta K} = K_{max}$, is obtained from Equation 2.27 [26].

For ductile materials, however, the value of γ for R<0 may be approximately equal to R $\geq$ 0 0 since, compressive loads contribute to crack propagation. Due to this fact, Walker's law appears with a modification in order to adjust to the experimental data applying a correction for values of R<0 expressed in Equation 2.30:

$$\begin{cases} \Delta K = \overline{\Delta K}(1-R)^{1-\gamma} \\ K_{max} = \overline{\Delta K}(1-R)^{\gamma-1} \end{cases} \implies \begin{cases} \frac{da}{dn} = C_W \left(\frac{\Delta K}{(1-R)^{1-\gamma}}\right)^{n_W} & R \geq 0 \\ \frac{da}{dn} = C_W \left(\frac{K_{max}}{(1-R)^{\gamma-1}}\right)^{n_W} & R < 0 \end{cases} \tag{2.30}$$

2.4.3 NASGRO equation

In the early 1980s, NASA developed a model for performing fracture control in manned space programs called NASGRO [27]. This model, contrary to the law from Paris and Walker, is able to model regions I and III, of da/dn curve, represented in figure 2.11, to take into account the effect of the stress ratio R and the effect of opening the crack. The NASGRO equation is given by:

$$\frac{da}{dn} = C_N \left[\left(\frac{1-f}{1-R}\right)\Delta K\right]^{n_F} \frac{[1-\frac{\Delta K_{th}}{\Delta K}]^p}{[1-\frac{\Delta K_{max}}{\Delta K_C}]^q} \tag{2.31}$$

In the expression above, C_N is a specific parameter for the NASGRO equation, although its value is the same as C_W in the Walker equation and C_P in the Paris law, it represents the ordinate at the origin, in a logarithmic reference, when R = 0. The parameter p is dimensionless and assists in modeling the da/dn curve for ΔK values close to the non-propagation limit (region I), q is also a dimensionless parameter that has an influence on the modeling of the propagation rate when K_{max} approaches the fracture toughness of the K_C material, (region III). The crack opening function, f, for the plasticity that induces the crack closure was defined by Newman. This R dependent function, is given by the fraction between the opening stress intensity K_{op} and the maximum stress intensity K_{max} during a cycle as shown in expression 2.32.

$$f = \frac{K_{op}}{K_{max}} = \begin{cases} max\left(R, A_0 + A_1 R + A_2 R^2 + A_3 R^3\right) & R \geq 0 \\ A_0 + A_1 R & -2 \leq R < 2 \\ A_0 - 2A_1 & R < -2 \end{cases} \tag{2.32}$$

The crack closure effect was discovered by Elber when investigating fatigue failures in load cycles of constant amplitude [28]. He observed that, during unloading, the crack was already closed before the minimum load was reached, or that the crack was kept closed until a certain level was reached, K_{op} as can be seen in Figure 2.13. The phenomena of crack closure has the consequence that not all the load ΔK contributes to the spread of the crack, but only an effective cyclic stress intensity, ΔK_{eff}.

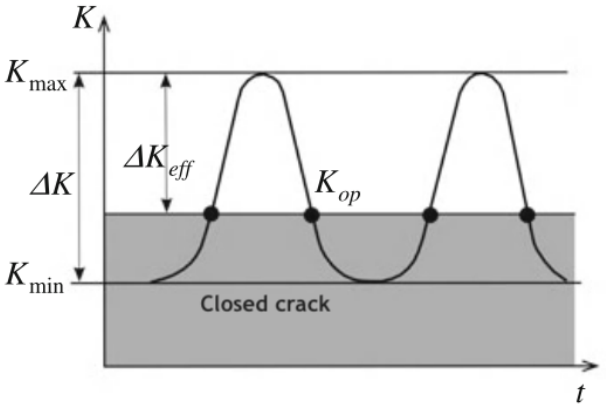

Figure 2.13: Crack closure effect [28] (adapted)

The dimensionless coefficients A_0, A_1, A_2 and A_3 are given by:

$$A_0 = \left(0.825 - 0.34\alpha + 0.05\alpha^2\right)\left[cos\left(\frac{\pi}{2}S_{max}/\sigma_0\right)\right]^{\frac{1}{\alpha}} \quad (2.33)$$

$$A_1 = (0.415 - 0.071\alpha)\,\frac{S_{max}}{\alpha} \quad (2.34)$$

$$A_2 = 1 - A_0 - A_1 - A_3 \quad (2.35)$$

$$A_3 = 2A_0 + A_1 - 1 \quad (2.36)$$

In the above equations, α is the stress / strain constraint factor and S_{max}/σ_0 is the ratio between the maximum applied stress (considering a cyclic external load) and the yield stress. In Equation 2.31, the non-propagation limit value ΔK_{th} is calculated by the following expression:

$$\Delta K_{th} = \Delta K_0 \frac{\left(\frac{a}{a+a_0}\right)^{0.5}}{\left(\frac{1-f}{(1-A_0)(1-R)}\right)^{(1+C_{th}R)}} \quad (2.37)$$

In the following expression, ΔK_0 represents the non-propagation limit value when $R = 0$, a_0 is the initial crack length, around $3.81 \times 10^{-5}[m]$ and C_{th} represents the coefficient initiation and assumes different values, depending on whether the stress ratio R is positive or negative.

The NASGRO model has the particularity that, through the critical value of the stress intensity factor K_{crit}, it includes the effect of thickness t, defined by the following expression:

$$\frac{K_C}{K_{IC}} = 1 + B_k e^{-(A_k \frac{t}{t_0})^2} \quad (2.38)$$

Where K_{IC} is the fracture toughness in a plane state of deformation for Mode I, A_k and B_k are adjustment parameters of the da/dN, and t_0 is the reference thickness, which corresponds to the plane state of deformation, given by:

$$t_0 = 2.5 \left(\frac{K_{IC}}{\sigma_Y} \right)^2 \quad (2.39)$$

2.5 Finite element method applied to fracture mechanics

The finite element method (FEM) is currently one of the most efficient methods of numerical calculation to solve problems in the engineering field, namely, it allows to model cracked components, calculate the stress intensity factor, K, and define boundary conditions. Their basic mathematical concepts are based on the work of Ritz et al in the early 20th century. The advancement of modern computer science in the 1960s allowed these approaches to be successfully implemented with this method. This development arose in large part due to structural analysis tasks in aviation, construction and mechanical engineering. The formulation of the finite element method as it is known today, was developed thanks to the pioneering work of Turner et al [28].

In the FEM, the geometry that is subjected to loads and restrictions is subdivided into small parts, called elements, which start to represent the continuous domain of the problem. This division into smaller elements allows to solve complex problems, subdividing them in simpler problems, allowing the computer to perform tasks efficiently. These divisions can have different geometries, such as triangular, quadratic among others, depending on the type and size of the problem.

As its definition suggests, as the elements have finite dimensions, they are called finite elements, a term that names the method. The elements are connected to each other by points, which are called nodes or nodal points. The set of all these elements and knots is called mesh. Due to these subdivisions of geometry, the mathematical equations that govern physical behavior will not be solved exactly, but approximately by this numerical method. The accuracy of the FEM depends on the number of nodes and elements, the size and types of elements of the mesh. That is, the smaller the size and the greater the number of them in a given mesh, the greater the precision in the analysis results, although with an increased computational cost.

2.5.1 Crack tip elements

According to Kuna [28], to obtain the best topology of a mesh, it must contain at least two regions with different refinements: the region surrounding the crack, defined by a refined mesh, and the remaining region of the material defined by a coarser mesh, called a regular mesh.

The unsatisfactory quality of the solution of the regular elements led to the development of special element formulations, in which the shape functions contain unique crack-specific functions, whose free parameters are related to the K factor, called crack tip elements. These are used to discretize the environment directly from the front of the crack, while regular elements are used to model the rest of the structure. For this model to allow good estimates of the stress intensity factor, there must be sufficient elements at the front of the crack ideally discretized in radial lines, usually in the form of a spider web made up of several concentric rings centered on the crack front as can be seen in Figure 2.14.

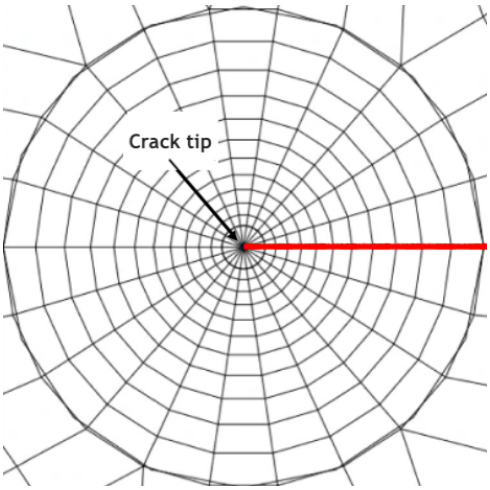

Figure 2.14: Mesh refinement in the crack front

At the crack tip, however, a singularity is observed in the stress field, as the radial distance in front of the crack r decreases, the local tension tends to infinity. The level of computational effort capable of modeling such a distribution with linear quadratic or hexahedral elements would be too high to obtain approximate results. Decisive progress has been made in this regard by the discovery of the so-called Quarter Point Elements. The basic idea is: in two-dimensional problems it leads to quadrilateral elements collapsing in triangles, as can be seen in Figure 2.15 (a). This switching leads to a convergence of nodes, leading to three nodes occupying the same position. In three-dimensional problems, there is a transformation of hexahedral elements into elements in wedge as shown in Figure 2.15 (b).

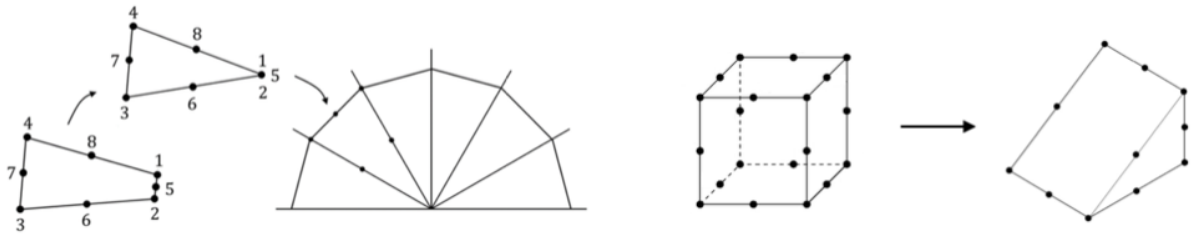

Figure 2.15: (a) Triangular element generated by collapse of quadrilateral element (b) transformation of hexahedral element into a wedge element [10] (adapted)

Considering only the elastic regime in the crack front, the nodes in the front of the crack (1,2 and 5) are normally collapsed and the intermediate nodes (6 and 8) are displaced at a distance $L/4$ of this, being L the lateral element length, as shown in Figure 2.16 . Thus, it is possible to model the singularity using the Jacobian transformation given by expression 2.40, which relates the variation of the displacement function u, in order of the x axis, with the radial distance r in front of the crack, in which c_0 and c_2 are constants that concern the geometry of the elements.

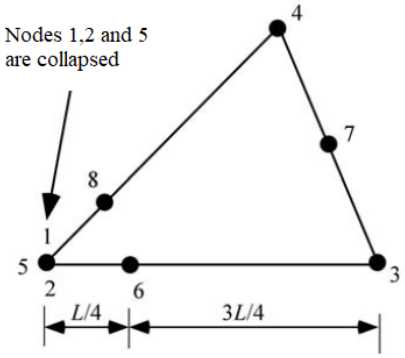

Figure 2.16: Element with elastic singularity [10]

$$\frac{du}{dx} = \frac{c_0}{\sqrt{r}} + c_2 \quad (2.40)$$

Such modification results in a singularity $1/\sqrt{r}$, which increases the numerical accuracy.

In the case of the existence of a plastic zone, the singularity $1/\sqrt{r}$ is no longer applied to the crack front. The element in this regime, like the elastic, is collected in a triangle, however, the knots in front of the crack are not collapsed and the location of the middle points (8 and 6) remains unchanged, at an $L/2$ distance as shown in Figure 2.17. The Jacobian of the transformation is given by the expression 2.41, where a singularity $1/r$ is generated [10].

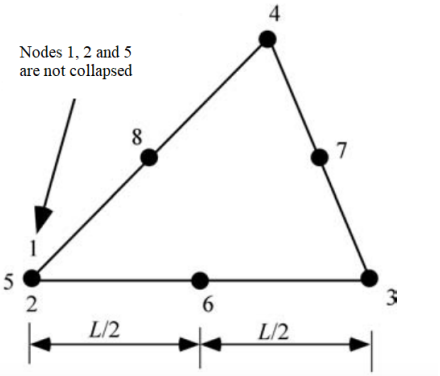

Figure 2.17: Element with plastic singularity [10]

$$\frac{du}{dx} = \frac{c_0}{r} + c_2 \quad (2.41)$$

Chapter 3

Finite Element Modelling

When dealing with three-dimensional and complex structures, its study through analytical methods becomes a complicated or even impossible task. The need to circumvent these restrictions led to the creation of numerical methods, which seek to present approximate solutions through the attribution of approximate functions, using error minimization criteria in detriment of exact solutions. Computers have revolutionized the practice of engineering, more specifically in design and analysis, with a large number of software, commercial and non-commercial, being developed in this sense.

Among all the computational tools for computer-aided engineering (CAE), the FEM is the most widely applied method or one of the most powerful modern ”calculators” available in the study of non linear structures. Softwares such as ANSYS®, ABAQUS®, NASTRAN®,BEASY®, StressCheck®, MODULEF®, among others, stand out in the use in Fracture Mechanics. In carrying out this dissertation, the author ended up choosing ANSYS®R19.2 due to the fact of being more familiar with the use of this software.

3.1 Methodology

In the context of the TB30 structural health monitoring (SHM) program, there remains a strong interest in the rigorous estimation of the accumulated damage to the Epsilon aircraft. Semi-elliptical surface cracks are among the most common failures in aircraft structures [29]. The growth of superficial cracks is responsible for a significant part of the fatigue life, requiring analyses of fatigue crack growth (FCG) pertinent to superficial cracks. In order for the FCG study to be reliable, it is essential to obtain an accurate stress intensity factor (SIF) expression that characterizes the geometry of the bulkhead.

The FE modeling aims to obtain the geometric factor of the Epsilon C2 reference that will later be used in the various propagation laws. Before moving on to the real structure, a simple experiment was performed with a cubic structure, which was previously conducted by Newman, in order to compare the results of the FEM with the analytical ones. This way we could prove whether our tool would give results with minimal error and thus move on to a more complex geometry.

Through the finite element method using the Ansys software, the crack propagation of the test structure was studied. For this purpose, the stress intensity factor K was calculated for various crack lengths, allowing to obtain the expression that describes the geometric factor Y ,represented in equation 2.14, as a function of the crack length. Subsequently, a propagation model carried out by J.Newman for NASA [30] was implemented in MATLAB in order to compare the obtained K´s in Ansys®with theoretical expressions, as well as the geometric factor Y.

3.1.1 Theoretical approach

An empirical solution of stress intensity factors for request mode *I* obtained from three-dimensional analysis in FE is proposed by Newman et al [30]. The equations were developed for a constant stress remotely applied to an elastic linear model and the front of the crack was modeled with elements that portray the singularity there. The stress intensity factor according to Newman for the geometry of Figure

3.1 is calculated according to the equation 3.1, valid for a a/b between 0.2 and 1 where S_t is the remote uniform tension stress, H_s is the bending multiplier for surface crack in a plate, S_b is the remote bending stress on outer fiber, Q represents the shape factor for elliptical crack and F_s the boundary-correction factor for surface crack in a plate under stress. The same source states that the empirical equations have an error of less than 5%.

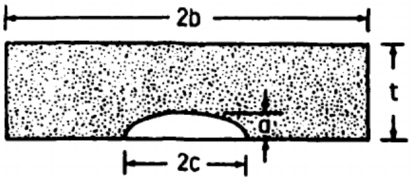

Figure 3.1: Newman nomenclature for semi-elliptical superficial crack, Newman et al[30]

$$K_I = (S_t + H_s S_b)\sqrt{\pi \frac{a}{Q}} F_s\left(\frac{a}{c}, \frac{a}{t}, \frac{c}{b}, \theta\right) \quad (3.1)$$

In order to apply the expressions for calculating K_I it is necessary that these conditions are met: $0 \leqslant a/c \leqslant 1$, $c/b < 0.5$ and $0 \leqslant \theta \leqslant \pi$. Thus, the K_I parameters are calculated according to expressions below 3.2 where g is a fine-tunlng curve-fitting function, f_θ is an angular function derived from embedded elliptical crack solution and f_w is a flnlte-width correction factor.

$$F_S = \left[M_1 + M_2\left(\frac{a}{t}\right)^2 + M_3\left(\frac{a}{t}\right)^2\right] g f_\theta f_W \quad (3.2)$$

$$M_1 = 1.13 - 0.09\left(\frac{a}{c}\right) \quad (3.3)$$

$$M_2 = -0.54 + \frac{0.89}{0.2 + \frac{a}{c}} \quad (3.4)$$

$$M_3 = 0.5 - \frac{1}{0.65 + \frac{a}{c}} + 14\left(1 - \frac{a}{c}\right)^{24} \quad (3.5)$$

$$g = 1 + \left[0.1 + 0.35\left(\frac{a}{t}\right)^2\right](1 - sin\theta)^2 \quad (3.6)$$

$$f_\theta = \left[\left(\frac{a}{c}\right)^2 cos^2\phi + sin^2\phi\right]^{\frac{1}{4}} \quad (3.7)$$

$$f_W = \left[sec\left(\frac{\pi c}{2b}\sqrt{\frac{a}{t}}\right)^{\frac{1}{2}}\right] \quad (3.8)$$

$$Q = 1 + 1.464\left(\frac{a}{c}\right)^{1.65} \quad (3.9)$$

3.1.2 CAD modelling

The simulation process, carried out using this software, is subject to three distinct stages, consisting on the Pre-Processing phase, followed by the Solution phase and, finally, the Post-Processing phase. In the first phase the geometry to be analyzed, the material model, the boundary conditions and the applied loads, the geometry and the crack parameters, as well as the finite element meshes are defined. In the solution phase, different types of analysis can be carried out. In the case of the present work, several static type analysis have been carried out. In this step, the program proceeds to obtain solutions of the system of equations using matrix calculation. Finally, in the Post-Processing phase, the results calculated in the Solution phase are presented.

3.1.3 Mechanical proprieties

Aluminum alloy is one of the leading materials in aeronautics due to its high strength, high elastic modulus and thermal resistance properties. In FE model, the material used for both structures is Aluminium alloy 2024-T351. The material's properties used were extracted from available bibliography and are listed in Table 3.1 [31].

Table 3.1: Material properties used on all calculations involving AA 2024-T3

Young's Modulus	Poisson's ratio	Density
73100 MPa	0.33	2540.2 kg/m^3

3.1.4 Boundary conditions and Loads

The main purpose of the boundary conditions is to constraint the model, thus influencing the degrees of freedom, which are generally characterized by translation and/or rotation. Since it is a static analysis, the boundary conditions must take into account that the body may suffer deformation with the application of loads, avoiding the occurrence of rigid body movement. For this, it is necessary to establish boundary conditions otherwise the model will generate a singular stiffness matrix, preventing its resolution, and stopping the simulation at the solution stage. The application of loads and boundary conditions affect the balance between the different elements that make up the mesh, inducing stress and deformation fields.

3.1.5 Finite Element Mesh

The results obtained through the FEM are severely influenced by the finite element mesh applied to the model. Factors such as number, distribution and geometry are crucial in the solution stage. At the same time, geometric features such as the presence of irregular shapes, notches, holes and sections with sudden changes in geometry should also be taken into account when applying the mesh to the model. The mesh must then be adapted to the type of analysis to be carried out and the geometric model to be studied must take into account details related to its construction so that the calculations are as reliable as possible.

3.2 Cube Model

A 10mm edge cube was initially modeled. A mesh was then generated where it was decided to use 10-node tetrahedron elements, these elements, have four corner nodes and six mid-edge nodes. Each node has three degrees of freedom (DOF), making a total of thirty DOFs in each element, as shown in Figure 3.2. Several studies show that tetrahedron elements may fit complex geometries very well with simpler computations with high level of accuracy [32] [33]. General meshing strategy using 10-node tetrahedron elements around the crack region is illustrated in Figure 3.4

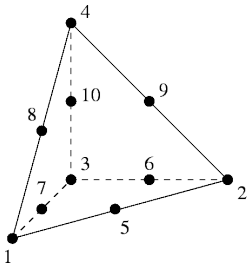

Figure 3.2: 10-node tetrahedral element

Once the mesh is defined and with the mechanical properties defined in Table 3.1 assigned, the structure acquires degrees of freedom of translation and rotation. The bottom of the cube was then fixed, i.e all degrees of freedom of the nodes in that face were totally restricted and a remote uniform tensile stress of 10MPa was applied on the top face of the cube.

With the primary conditions already defined, a semi-elliptical fracture was inserted in one face as shown in Fig3.3. Due to the nature of the geometry of this crack, it is important to describe the position of a certain point on its front in a polar reference, where, (r, θ) are radial and angular coordinates, respectively, with the origin located at the crack-front. In order to comply with the requirements presented in Section 2.6.1, regarding the elements in front of the crack and taking into account the geometry of the crack and the structure, a circular offset of $0.2mm$ around the crack was created. This offset includes eight contours that allow obtaining eight estimates for stress intensity values related to the failure mode I.

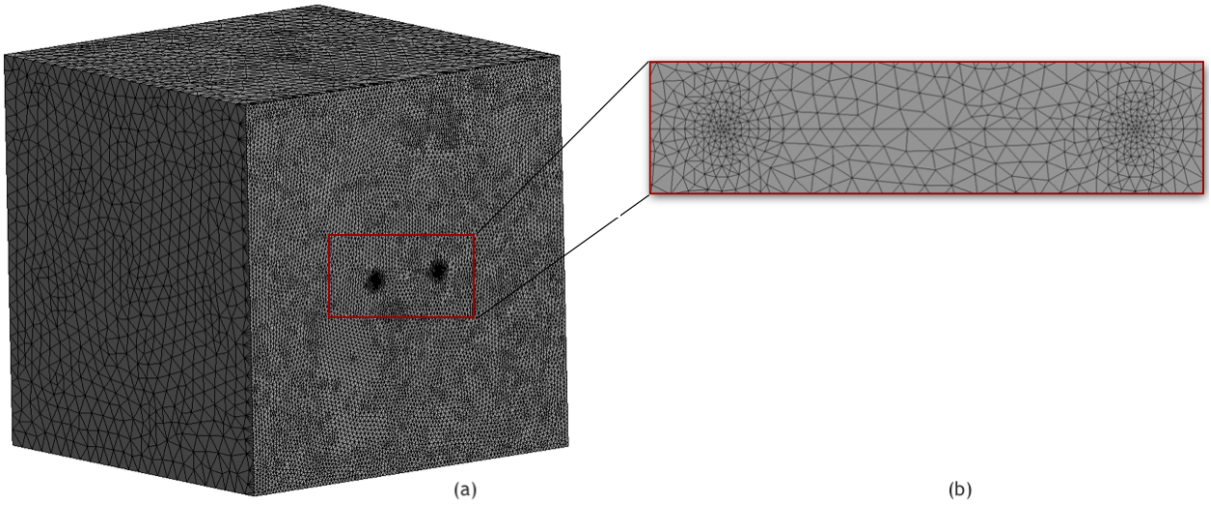

Figure 3.3: (a) Finite Element mesh cube (b) crack mesh and contours

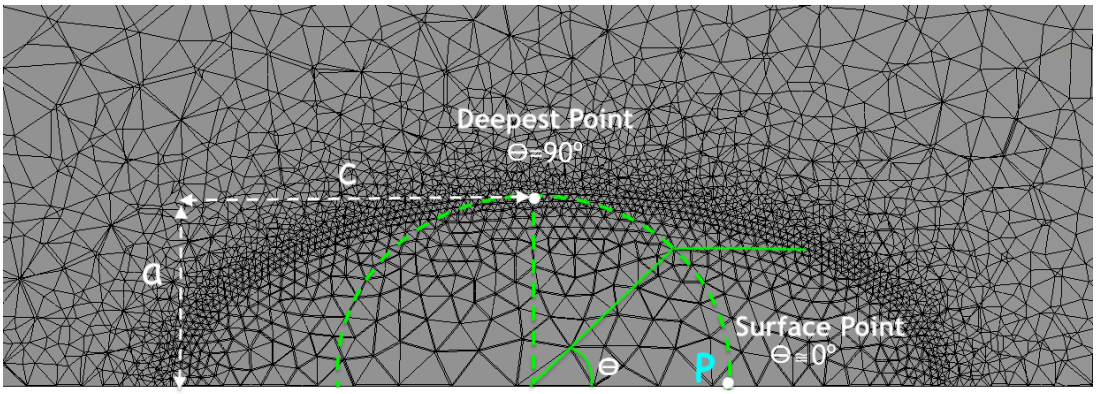

Figure 3.4: Meshing strategy around the crack front

A range of crack lengths between 0.5mm and 1.4mm was also defined in 0.1mm increments, making a total of 12 crack lengths. In this way, it was assumed that the shape of the crack remains constant throughout the propagation, forming a crack with the shape of a semi-ellipse, in which the angle θ varies between 0 rad and θ rad. From the ANSYS simulation, the different K values for the several countours were averaged, in order to obtain more reliable values for the stress intensity factor, for the different crack lengths. These values were compared with the model developed by Newman [30], illustrated in Fig 3.5, for a surface crack and subject to a tensile load. It was assumed that $c = 2a$ to maintain the crack in a semi elliptical shape.

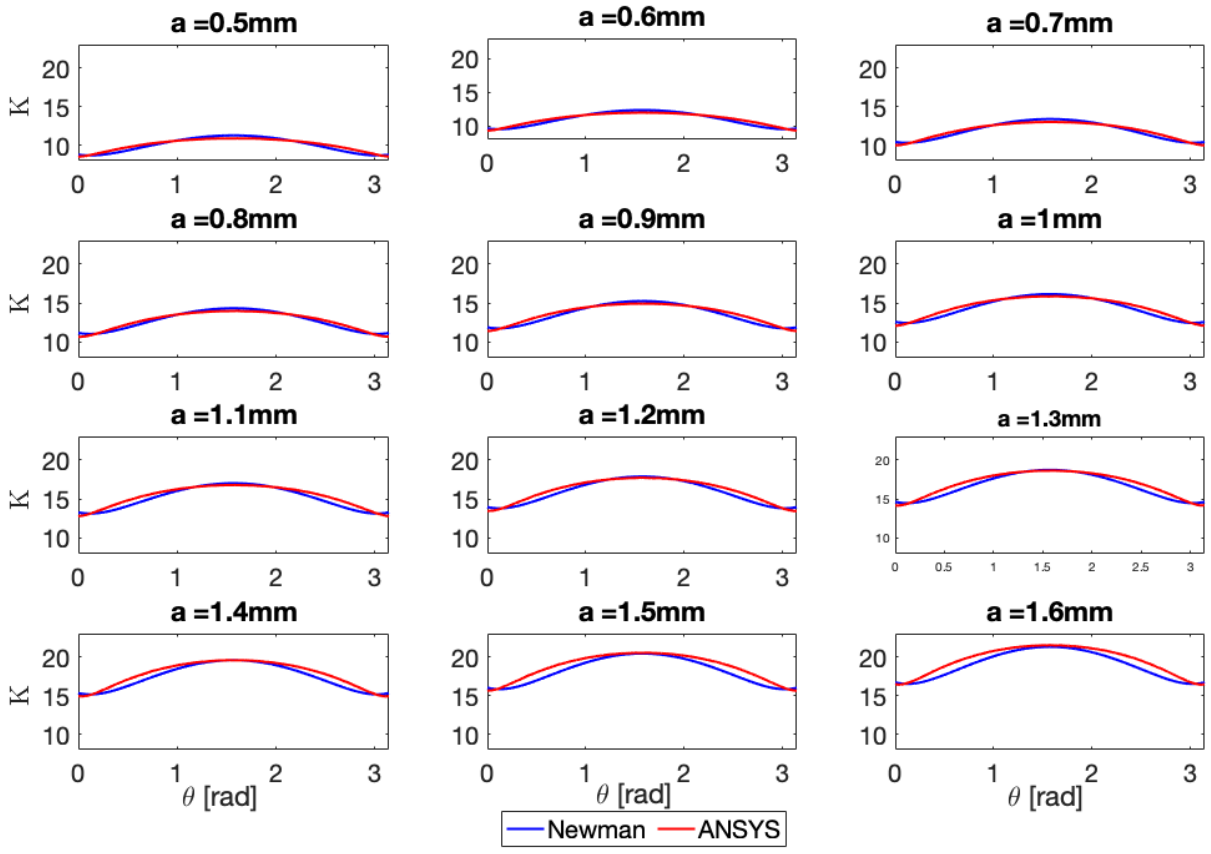

Figure 3.5: Comparison of K value with Newman's model along the crack front of a semi-elliptical surface crack.

The results shown in Figure 3.5 show the expected increase in the value of K_I with the growth of the size of the crack. It is also possible to observe that the curve referring to the K_I values for both analyses presents a relatively similar behavior. In both curves there is a symmetric behaviour relative to $\theta = \frac{\pi}{2}$ due to the fact that it has been assumed that the shape of the crack remains constant. The K-value at the deepest point ($\theta = \frac{\pi}{2}$) is significantly larger than at the material surface. The fatigue crack growth in the depth direction will then be faster than along the crack front.

Comparing the values of the SIF, the deviation between the results of the FEM and the Newman model is shown in Table 3.6. In general, the results are satisfactory since the error does not exceed 5% between the two analyses. That said, it is possible to validate the proposed methodology, when compared with the model developed by Newman.

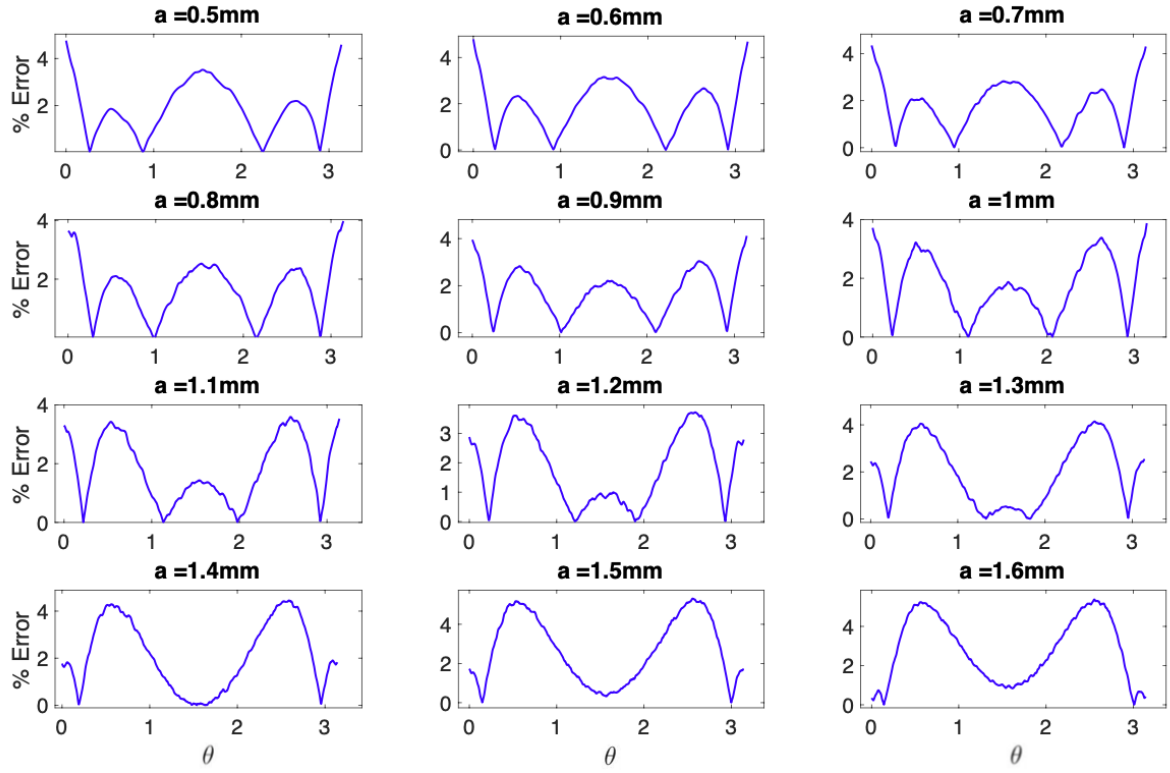

Figure 3.6: Error between Newman's and Ansys K values

3.2.1 Geometric parameter Y

With the values of stress intensity factor obtained, which characterize the conditions of geometry and stress in front of the crack, the geometric parameter Y was determined. Assuming that the shape of the crack remains constant, presenting a crack length independent of the angular position θ, it was decided to calculate the average value of the stress intensity factor K_I for each crack length. For the determination of the geometric parameter Y, the values of the SIF for the various crack lengths were sized according to the equation.3.10.

$$Y = \frac{K}{\sigma\sqrt{\pi a}} \quad (3.10)$$

Then, using Matlab®*Curve Fitting Toolbox*, the expression of the geometric parameter along the front

of the crack was determined through a 4th degree polynomial regression, due to the fact of being the lowest degree that guaranteed a good fitting. In Figure 3.7 the 3D surface plot is depicted as well as the corresponding expression of the geometric parameter Y in Equation 3.11. , being valid for crack lengths between 0.5mm and 1.6mm. The quality of a fitting is ensured by the coefficient of determination R^2, which is proportional to the variance of the data. When $R^2 = 1$ the variance is null therefore the fitting perfectly adjusts to the experimental data. In this case the value for R^2 obtained was 0.99, validating the polynomial regression.

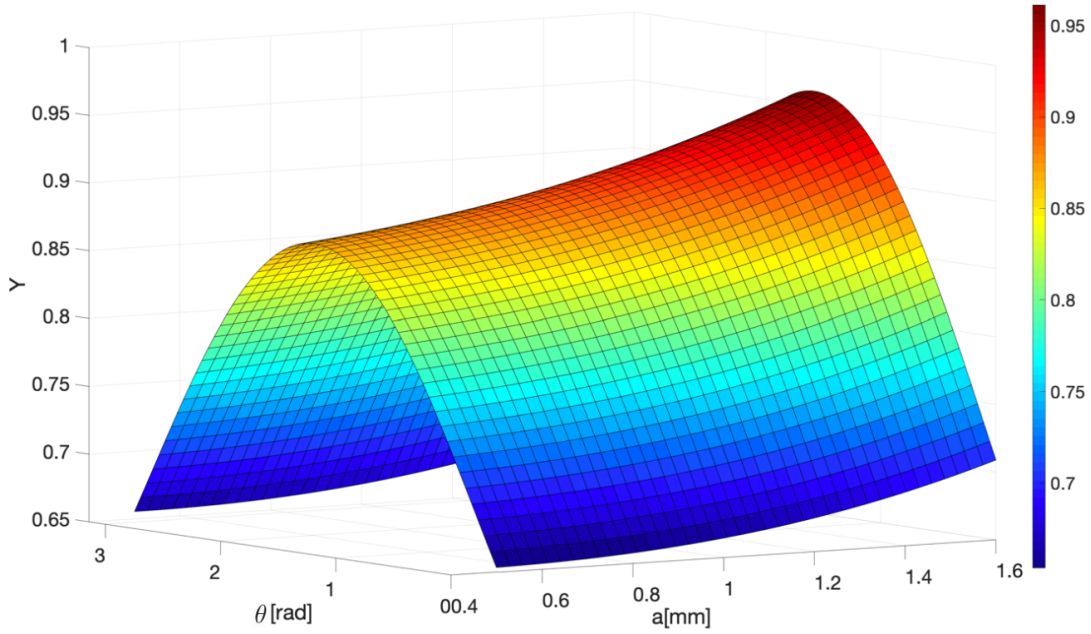

Figure 3.7: Surface Plot - Geometric Factor

$$\begin{aligned} Y(a,\theta) = &-0.0028644a^4 - 0.00070748a^3\theta + 0.022928a^3 + 0.00083483a^2\theta^2 + 0.00021213a^2\theta \\ &-0.0039489a^2 + 0.00018322a\theta^3 - 0.015214a\theta^2 + 0.042094a\theta - 0.0072162a \\ &+0.009451\theta^4 - 0.059918\theta^3 + 0.037654\theta^2 + 0.18197\theta + 0.6554 \end{aligned} \tag{3.11}$$

Then, in order to make a comparison between the experimental and theoretical model, the statistical distribution of the experimental error was determined. To do so, a stochastic analysis was conducted, where n random combinations of (a, θ) were generated. Afterwards, these values served as input to compute both $Y(a, \theta)$ and $Y_{theor}(a, \theta)$ which is the theoretical expression obtained from Newman model values then used to obtain the error distribution [30]. For the visualization of the error a box plot was created as shown in Figure 3.8

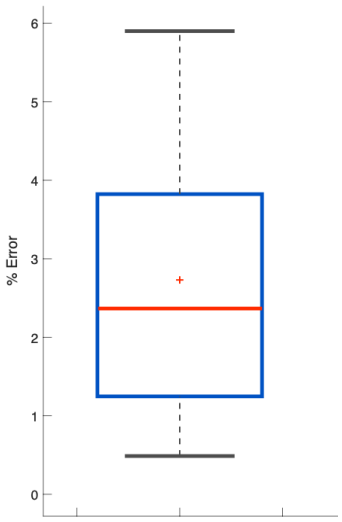

Figure 3.8: Box plot of %Error of experimental model

For the elaboration of this box plot, $n = 10.000$ of random combinations of (a, θ) were used. It is possible to observe that the average error is placed at 2.4% and the interquartile range is comprised between 1.2% and 3.9%. Despite some values are shortly above 5%, they are placed at the tail of the distribution and therefore are less likely to occur. These higher values occur at the free surface, $\theta = 0$ and $\theta = \pi$. The respective box plots showing the error in these locations are shown in the Figure 3.9. According to studies carried out, the singularity of the stress on the free surface, point P in Fig3.4, is not proportional to $\sqrt{r}$ (r being the distance from the crack tip). In concrete terms, the concept K, and consequently Y, is not completely valid at point P, therefore, explaining these obtained discrepancies [34]. In general, the errors obtained between the two methods are minimal and it is then possible to validate the methodology developed by Newman regarding semi-elliptical cracks in the surface subjected to uniform load.

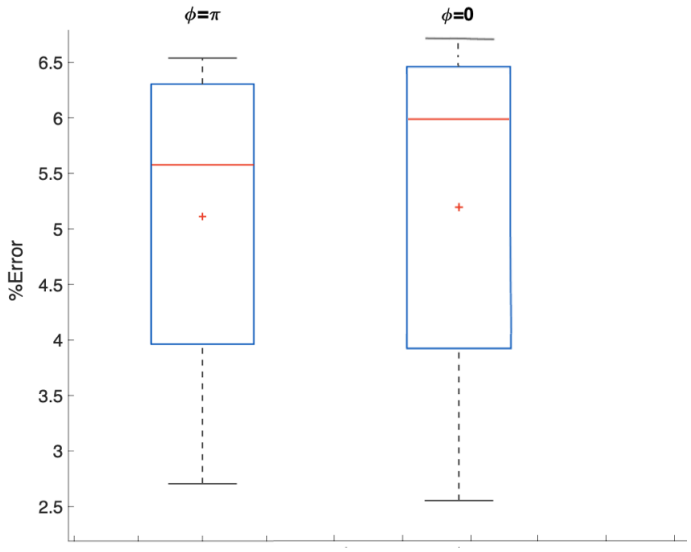

Figure 3.9: Box plot of % Error of experimental model

3.3 Real Structure

In Figure 3.10 a detailed airframe of the Epsilon TB-30 aircraft is depicted. This airframe is composed by the wings, the fuselage and the stabilizers. The wing structure assembly is composed by the two wings attached to frames in each wing mainly consists of a main spar, a rear small spar, 12 ribs and by an outer metal skin. The fuselage structure assembly is composed of 11 frames, 4 spars and the outer metal skin.

After full scale tests carried out at CEAT, on this aircraft, it was determined that the critical component for determining the aircraft's useful life was Frame C2. This frame, helped by a smaller Frame C3, form the main connection between the fuselage and the wing structure.

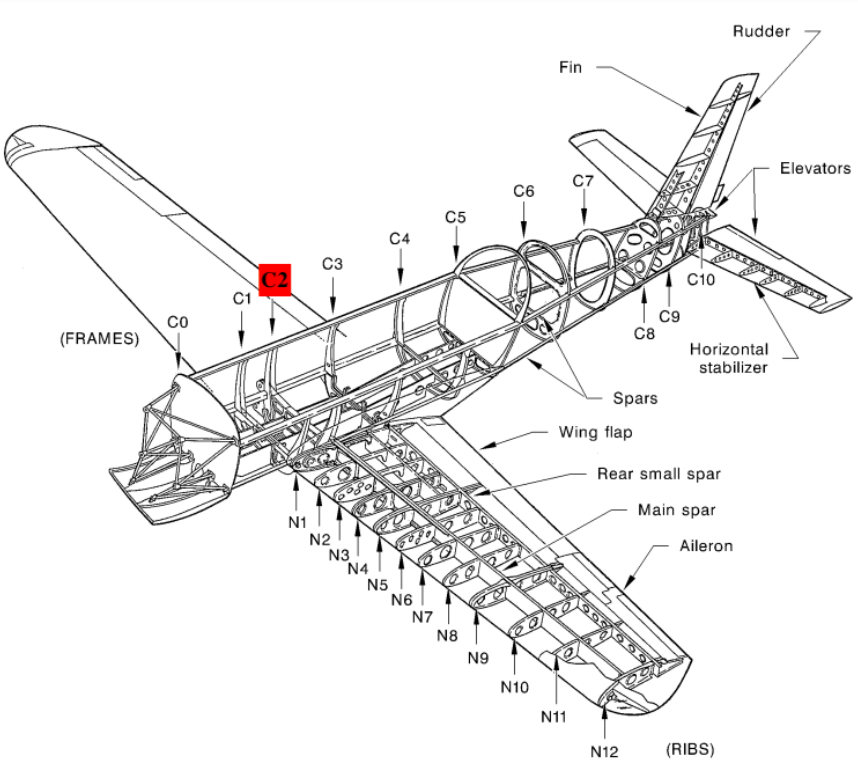

Figure 3.10: Epsilon TB-30 Airframe [35]

The CAD model of the spar and frame was obtained by Martins [7] through reverse engineering. It was then imported into Ansys where the assembly of these two structures was done so that the study was as close as possible to the real situation. The connection from wing to the fuselage must be highly durable to withstand all the loads applied to it. This connection (lug structure) is also responsible for transferring the bending moment and shear loads acting on the wing to the fuselage. Lugs are connector type elements used as structural supports for pin connections. Each side of the frame structure has three lugs in which each consists of two holes together with an integrated upper flange and a lower flange that will be connected to the two wing spar lugs, as so is depicted in figure 3.11. A tightly fitted $25\ mm$ diameter structural steel pin was then created and inserted through the aligned holes.

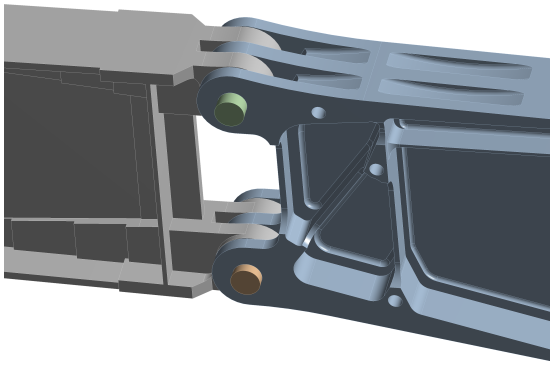

Figure 3.11: (CAD model) Bolted connection between Frame C2 and Main wing Spar

3.3.1 Mechanical Properties

After defining the geometry to be studied, the mechanical properties of the material were defined. The airframe of the aircraft under study is made of aluminum alloy 2024-T351, the properties shown in Table 3.2 were used [31] .

Table 3.2: Aluminum alloy 2024-T351 mechanical properties

Mechanical Properties	**Values**
Tensile strength (σ_{UTS})	469 MPa
Young's modulus (E)	73100 MPa
Poisson coefficient (ν)	0.33
Fracture toughness - plane stress state (K_c)	84.611 $MPa\sqrt{m}$
Fracture toughness - plane strain state (K_{IC})	37.361 $MPa\sqrt{m}$
Yield stress (σ_Y)	324 MPa

3.3.2 Considerations

In order to simulate and model aeronautical components correctly and close to the real, it is necessary to take into account some principles of flight mechanics. The weight of the aircraft W_a is always directed to the center of the Earth acting on the aircraft's center of gravity. Its magnitude depends on the mass of all parts of the aircraft, the amount of fuel, plus any payload. For this case, the maximum service mass of the aircraft is 1300kg so that the assumed weight of the aircraft should be in all flight situations for the calculations performed, in order to achieve conservative results.

For this study we considered the case in which the aircraft is subject to a unit load factor and performing straight-and-level and unaccelerated flight, that is when all the forces that act on the airplane are in static equilibrium, Lift (L) equals Weight (W_a) and Thrust (T) equals Drag (D), as is given by Equations 3.12 and 3.13. It was assumed that the vertical forces applied to the aircraft in level flight are those represented in Figure 3.12, in which we can observe the lift generated by the wings L_w that is applied to the aerodynamic center of it, the lift generated by the horizontal stabilizer L_t, applied to its aerodynamic center, and the weight of the aircraft W_a that acts on the CG of it. The distances from the aerodynamic center of the wing and the aerodynamic center of the horizontal stabilizer to the aircraft CG are, respectively, l_{cgw}=$58mm$ and l_{cgt}=$4464mm$. Since only vertical data will be provided, horizontal forces such as Drag (D) and Thrust (T) will be of little interest for this study and thus their contribution to damage is to be considered neglected.

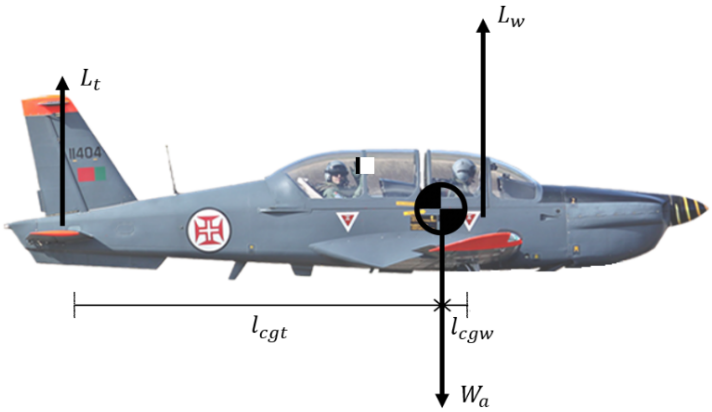

$$\sum F_z = 0 \Leftrightarrow L = W_a \quad (3.12)$$

$$\sum F_x = 0 \Leftrightarrow T = D \quad (3.13)$$

Figure 3.12: Aircraft Free Body Diagram in Steady Level Flight[8]

For the determination of the stress located in the critical zone previously mentioned, Frame C2, we started by assuming that the wings are subject to an elliptical lift distribution $L_d(x)$ as illustrated in Figure 3.13 and described by the Equation 3.14

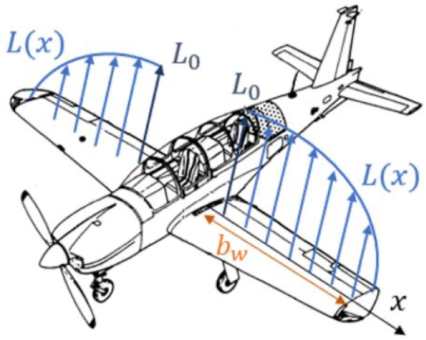

$$L_d(x) = L_0\sqrt{1-\left(\frac{x}{b_w}\right)^2} \quad (3.14)$$

Figure 3.13: Elliptic Lift Distribution [8]

In this equation there are two parameters: b_w which is the length of one spar and L_0 which is the lift value at the root of the wings. For the obtention of L_0 we set the equilibrium of the vertical forces, applied on the aircraft, as well as the balance of moments, around the CG, considering that it is a level flight, the load factor has a unit value of $n_z = 1$. This equilibrium is described by the system of Equations 3.15.

$$\begin{cases} W_a = L_w + L_t \\ L_w l_{cgw} - L_t l_{cgt} = 0 \end{cases} \quad (3.15)$$

The lift of the wing L_t and of the horizontal stabilizer L_w are given by the Expressions 3.16 and 3.17 respectively.

$$L_t = \frac{1}{2}\rho C_{L_t} S_t V_e^2, \quad (3.16)$$

$$L_w = \frac{1}{2}\rho C_{L_w} S_w V_e^2 \quad (3.17)$$

Substituting Expressions 3.16 in the Equation system 3.15 and knowing that the aircraft has an approximate mass of 1250 kg, the values of the lift force for the wing and for the horizontal stabilizer are respectively $L_w = 12105N$ and $L_t = 157N$. Then, through Equation 3.18 we obtain the value of $L_0 = 2527N$.

$$2 \times \int_0^{b_w} L(x)dx = L_W \Rightarrow L_0 = 2527N/m \quad (3.18)$$

3.3.3 CAD Model

Despite the powerful parametric tools available in CAD packages, the responsibility for creating efficient and true-to-life models that can be easily modified still rests with the user. In this sense, identifying which modeling best practise is most appropriate for a specific design situation and understanding how the design tree can be structured are critical factors to ensure an efficient simulation. Therefore, it is essential to select a well thought out modeling methodology to ensure an efficient functional model and minimize the time and effort involved in making changes based on the characteristics and requirements of the real model.

3.3.4 Loading conditions

Since the values of the horizontal forces acting on the aircraft cannot be easily determined with the data available and considering that their influence on the structural integrity of the aircraft structure is reduced compared to vertical forces, only these last ones will be considered.

Taking into account that the lift on an aircraft is mainly generated on the wings, a force of variable magnitude governed by Equation 3.14 was only applied on the upper surface of the spars, knowing however, that part of the lift is created by the skin that involves the structure. Analyzing Equation 3.14, it is possible to observe that on an wing with an elliptical lift distribution, lift (L), reaches its maximum value, L_0, at the root of the wing and decays to 0 near the wing tip. Although an elliptical lift distribution has been used, it may be very different from the real wing lift distribution, since it still does not take into account several geometric factors, such as chord distribution, torsion and dihedral.

An axis was created whose origin was strategically placed in the wing root so that the x axis was pointing along the span, in accordance with the equation, as represented in Figure 3.14.

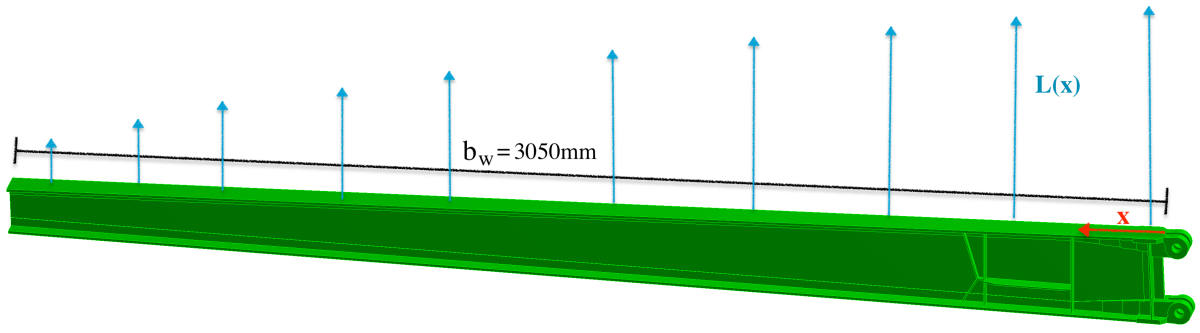

Figure 3.14: Wing Spar CAD model

3.3.5 Constraints

With the load application conditions already defined, it was necessary to apply displacement restrictions to produce a static analysis for Frame C2. In order to reduce the required computational power and thus

facilitate each simulation and once the structure has a symmetry, it was decided to split the structure under study in half. The simulation of boundary conditions and other forms of constraint is probably the most challenging part of the accurate modeling of a structure for a finite element analysis. In specifying constraints, it is relatively easy to make mistakes of omission or misrepresentation. It was then necessary to test different approaches to model trustworthy constraints which required a lot of computational time. The boundary conditions applied to the model were varied to obtain the results that most accurately represented real observations.

The contacts between the wing spar, the frame and the pins were initially established. It was considered that the spar structure would be somehow fixed to the frame and that is why fixed joint connections were created to connect the components, but still allowing deformations to transmit through both structures. Subsequently, with the loads and connections already established, it was necessary to impose restrictions to prevent the model from behaving like a free body. As previously mentioned, once the model has a symmetry, it was divided in half as shown in Figure 3.15, and so a remote displacement was applied to the nodes in the green sliced face where the degrees of freedom of rotation and translation were restricted.

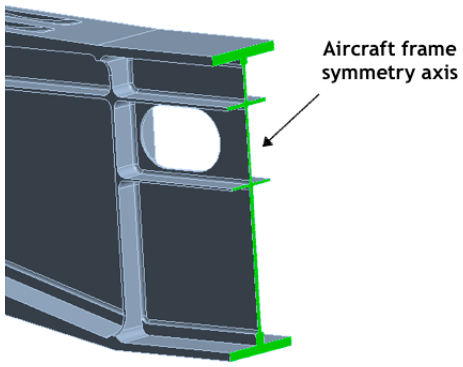

Figure 3.15: Detail of the cut zone on the aircraft frame symmetry axis

3.3.6 Mesh

As stated before, in order to conduct a finite element analysis the structure must first be idealised into some form of mesh. As the method is approximate it is necessary to have a good idea of the expected solution, together with an understanding of the consequences of the assumptions made with the element types to be used. This allows the effects of the approximation to be minimised within the solution. Before a FE mesh can be specified the problem that is to be analysed must first be identified. This requires that four blocks of information are defined: the geometry, the boundary conditions, the loadings and the required results.

Mesh properties such as the mesh density and the element shape quality are important factors that affect the solution accuracy and efficiency. Finer mesh is usually needed in areas where high stress/strain rates are expected. The type of finite element employed also plays a vital role in the analysis. Most general purpose FE programs provide the user with a wide range of choice as to the element types that can be used so that the user can use whatever is most appropriate for the problem at hand. However, for any program, there are elements that are recommended for certain analyses. Since we are facing a problem of crack propagation and the software in use is Ansys there are certain conditions that must be respected. This software requires that in the body part of the structure where a crack is inserted a mesh with tetrahedric

elements should be applied. As noted before, tetrahedral elements are a much more adaptable shape than octahedral elements and allow to tailor the element mesh in many ways to suit any structural geometry or to anticipate any likely distribution of stress concentration. For that reason, it was decided to apply the same kind of elements throughout the all structure, and at least three elements through the thickness.

Mesh generation is the basic step in any simulation, although the software typically cannot obtain exact solutions for models, it can find highly accurate approximations. In practice of finite element stress analysis, first it is mandatory to know if key stresses are converging, and second if they have converged to a reasonable level of accuracy. In order to achieve results that are reliable when using the finite element method, it must be ensured that an acceptable mesh is used with respect to the shape and size of the elements. A mesh convergence study is performed to make sure that element sizes are sufficiently small such that the solution obtained using finite element analysis is accurate to a desired level. As we keep on increasing the number of elements, the problem requires more and more computational resources, so both the computational cost and desired accuracy were considered while generating a mesh. The convergence study was conducted on several mesh sizes to obtain an estimate of the variation in Von Mises stresses until it reached a point where the variation between the stress values had a difference close to 1% as is depicted in Figure 3.16.

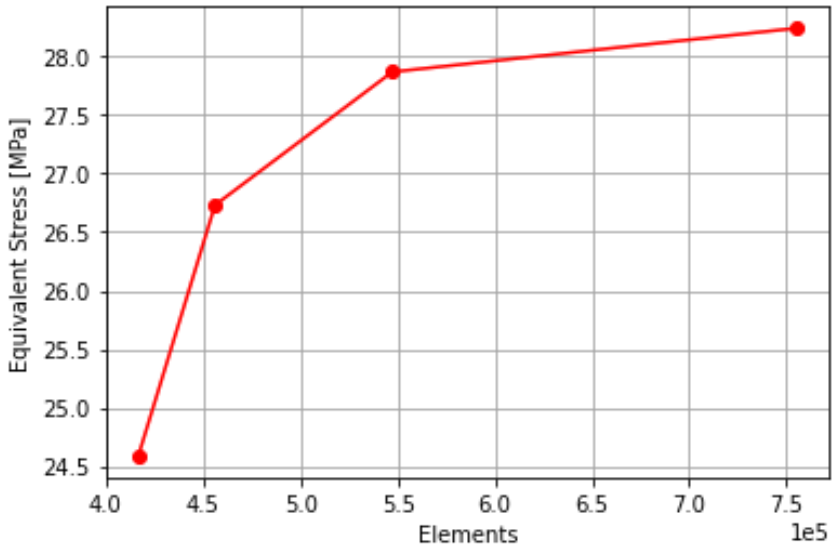

Figure 3.16: Convergence study performed on C2 Frame critical spot

The solution was found to be reasonably converged at overall mesh with $8mm$ elements in the main wing spar and a $4mm$ mesh in the frame. Since this study focuses mainly on the frame structure, in sections with more complex geometry bordering critical regions, the mesh has been refined to$2mm$ elements and even smaller in critical regions like represented in Figure 3.19.

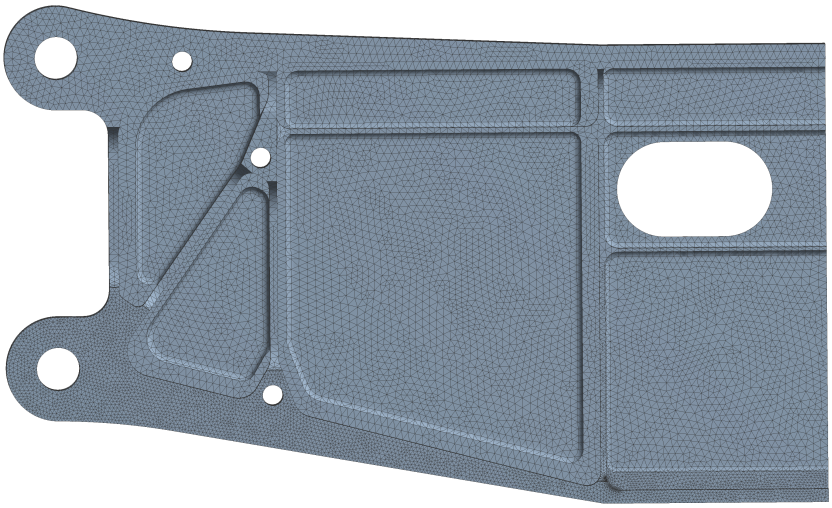

Figure 3.17: Finite element mesh of Frame C2

Figure 3.18: Finite element mesh of the Main wing spar with magnified area

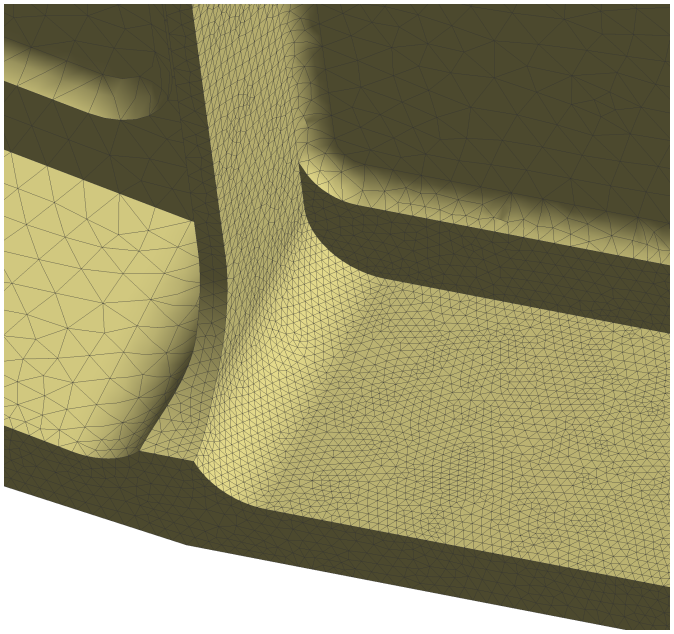

Figure 3.19: Detail of the finite element mesh of the frame

3.3.7 High Stress Location

From the CEAT [2] report, crack growth was detected from a stress hotspot located at the root of the innermost ribs in frame C2, as shown in Figure 3.20. In addition, previous works carried out in the context of monitoring the fatigue of the PrtAF Epsilon TB-30 aircraft also supported this statement, reaching the same conclusion and so confirming this result [7].

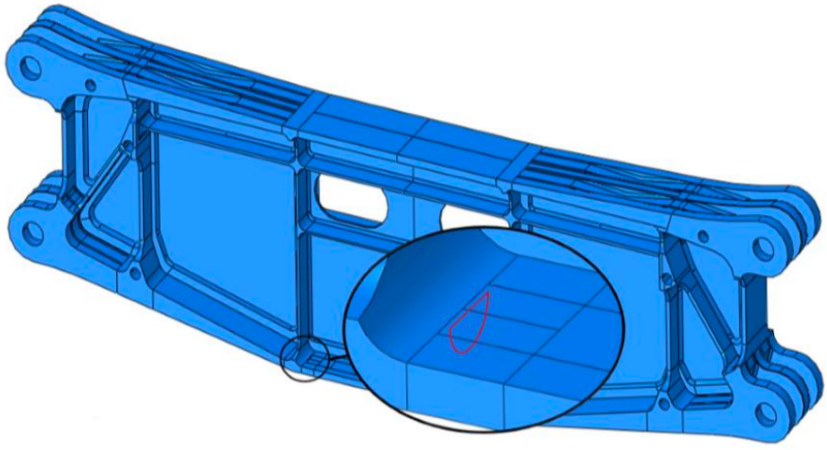

Figure 3.20: Frame 2 CAD model [7]

While simulations were being carried out, these results were always taken into account in order to achieve similar and reliable results before moving on to the insertion and study phase of crack propagation in the structure.

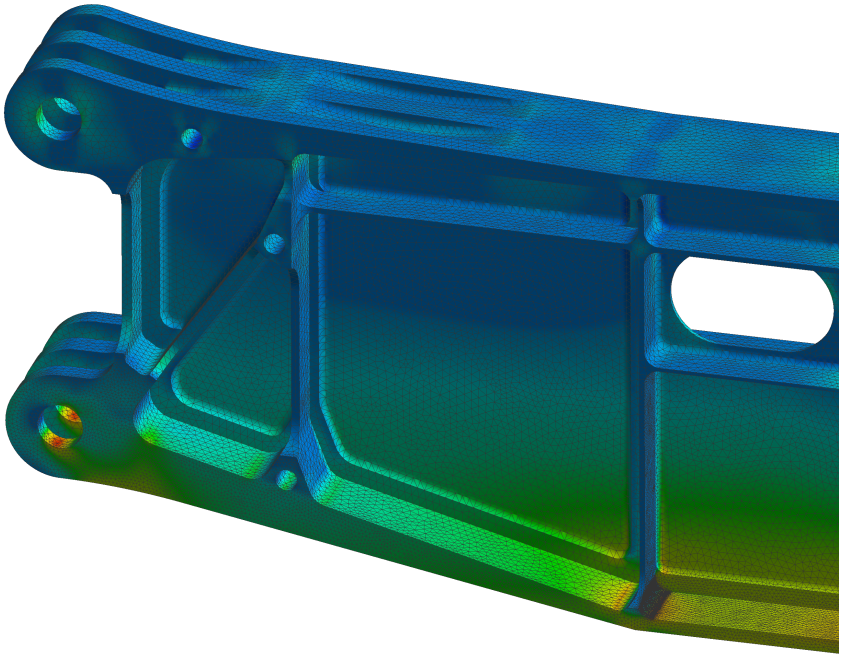

Figure 3.21: Principal Stress distribution on C2 Frame

Figure 3.21 represents the Ansys result that was considered acceptable, in part to those reported, in relation to the stress distribution in the frame, taking into account, in particular, to the maximum stress located at the root of the innermost ribs in frame C2 where the crack will be inserted. Regarding the value of the stress for this critical hot spot shown in Figure 3.22, the magnitude of the stress obtained was 33.7 MPa which was then compared with recent measured values retrieved from PRODDIA® AERO software [36]. This software, developed by the firm Stratosphere SA, receives and handles flight data from the instrumented aircraft within the scope of the SHMTB30 program. Then, a comparative study of the stress intensity factor obtained in the simulation with those that are actually felt in the aircraft structure was made. It was possible, with the results, to conclude that these showed a trusty behavior with a a

relatively low error.

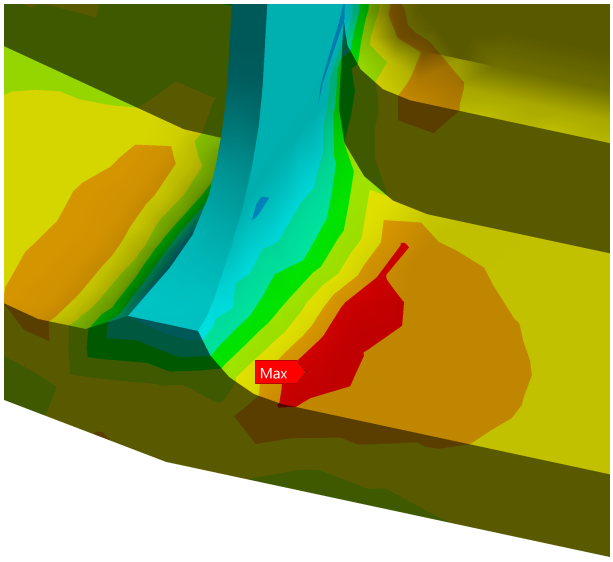

Figure 3.22: Maximum Principal Stress detail

3.3.8 Crack geometry

In the analysis environment, to ensure the exact position of the crack surface body and define the crack tip and crack growth direction, a coordinate system ought to be set before analysis. The x-axis of the created coordinate system should point to crack growth direction or crack tip and y-axis should be perpendicular to the crack surface. Because of using contour integral method to calculate relevant property parameters of crack is used, the number of contours and crack tip elements should be pointed in order to improve computational accuracy so that the crack can be inserted into the whole structure body successfully. The centre of the semi elliptical geometry of the crack should, ideally, be positioned in the exact point of maximum stress but because of the complexity of the filleted area, an offset of $1mm$ was made along the y-axis as depicted in Figure 3.23.

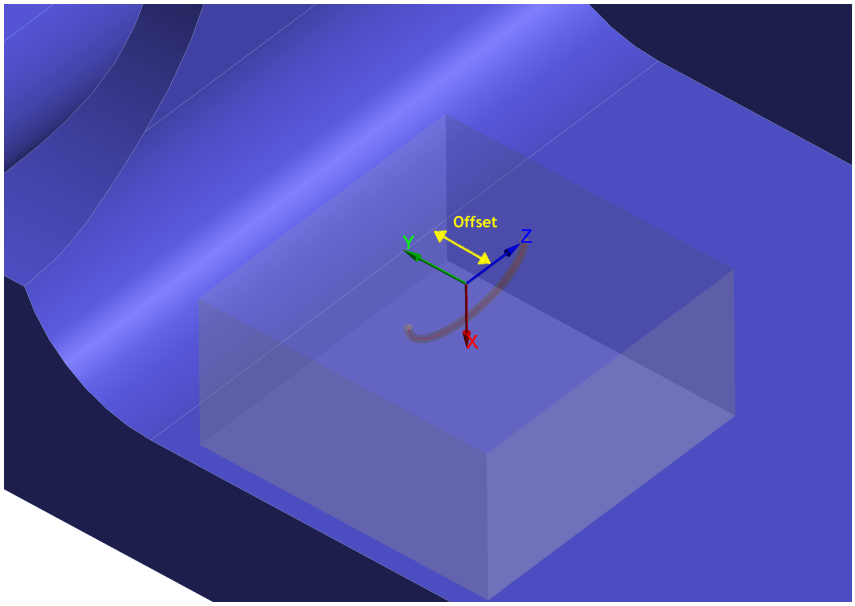

Figure 3.23: Location of the crack on the C2 Frame

Similar to the study performed on the cubic structure, a semi-elliptical crack was created using the same polar reference. It is important to note that this geometry was created and parameterized in the sense that it can be generated automatically for any crack value between $0.2mm$ and $6.4mm$, since the region where the crack was inserted has a thickness of $7.3mm$. Due to the tolerances of the software, the precision of the increments of the crack should not exceed a tenth of a millimeter.

Due to the crack tip singularity, a refined mesh should be generated surrounding this area in order to derive reliable stress intensity factor results. To ensure that the crack surface was correctly modelled, when it comes to size and shape, a mesh, represented in Figure 3.24, was created with a uniform size of $0.5mm$ and $1mm$ in the surrounding regions that are in contact with the region under study.

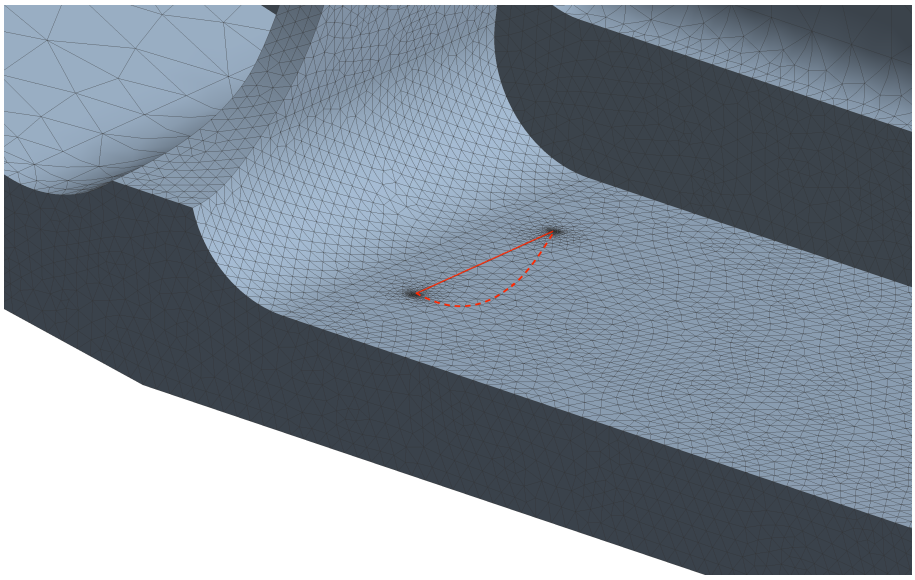

Figure 3.24: Crack surface (in red)

The contour radius, showed in Figure 3.25, define the size of the affected zone of the fracture by meshing around the crack front and corner points. This radius was taken to be $0.5mm$ in order to generate ultra-fine meshing around the crack front and 6 contours were included. Due to the stress singularity point at the crack tip and the fact that ANSYS uses the integral contour method to calculate the stress intensity factor, the accuracy of the solution is affected. Therefore, it is convenient to choose the results obtained from the second to the sixth contour.

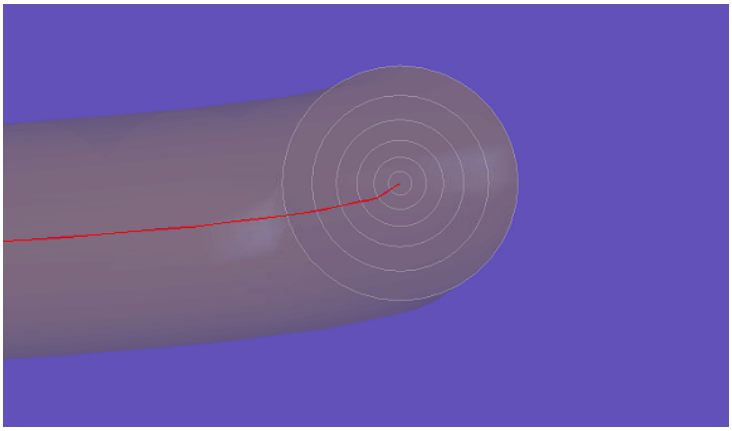

Figure 3.25: Detail of the 6 contours surrounding the crack

3.3.9 Determination of Stress Intensity Factors and geometry factor

By averaging the K-values obtained at the various contours, for each crack size, it is possible to obtain representative SIF values for each point along the crack front. Regardless of the modeling method of the crack, for a superficial crack of semi-elliptical geometry, subjected to stress mode I, the total maximum stress position distributes on the deepest location of the crack tip and minimum stress position distributes on the opening location at the two ends of the crack. A representation of this behaviour is given by Figure 3.26 which provides the stress distribution along the crack for $a = 0.6mm$.

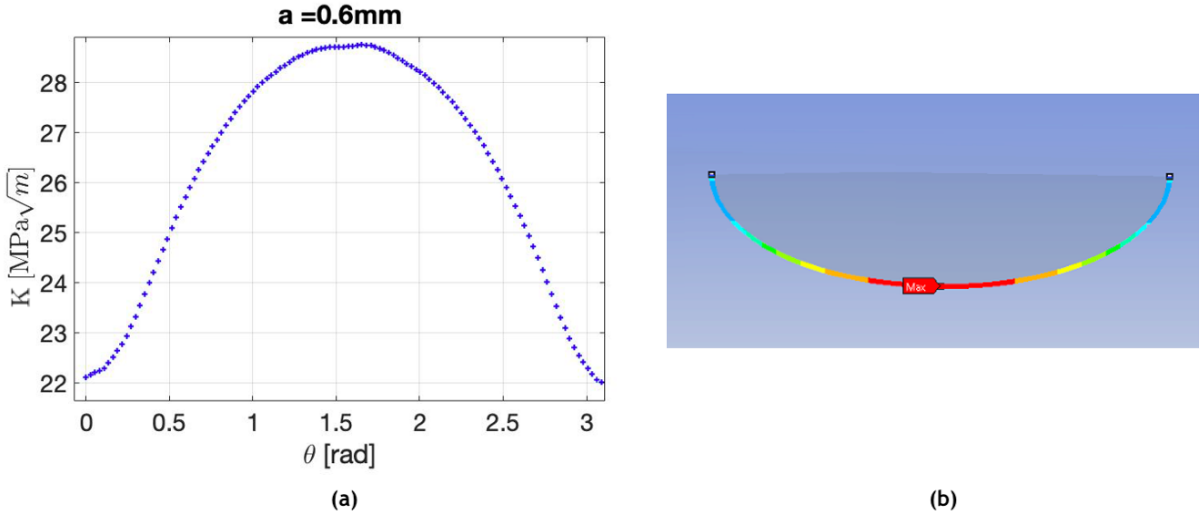

Figure 3.26: (a) K values obtained from Ansys for a=$0.6mm$ (b) Distribution of stress along the crack front (Ansys)

Although theoretically this curve should have a symmetry at θ = $\pi/2$ and would present the maximum stress at that angle, as shown on the left side, for any crack size, the truth is that as the crack size increases, this curve no longer exhibits this behavior. In reality, for bigger crack lengths, the curve is not symmetrical and reveals lower SIF values on the side of the crack nearest to the central rib of the structure and is likely caused from the apparent decrease in stress close to the rib since the structure is not symmetrical with respect to the crack front 3.22.

Similarly to the study done on the cube, for the propagation analysis we simulated a variety of crack sizes ranging from $0.2mm$ to $4mm$ in $0.2mm$ increments. It was also assumed, a priori, that the crack would maintain its original semi-elliptical shape throughout. For each crack size, the values of K obtained in Ansys were exported. Then, by resorting to Matlab, a surface plot in 3D for better visualisation of the behavior of K in relation to the parameters θ and a was made.

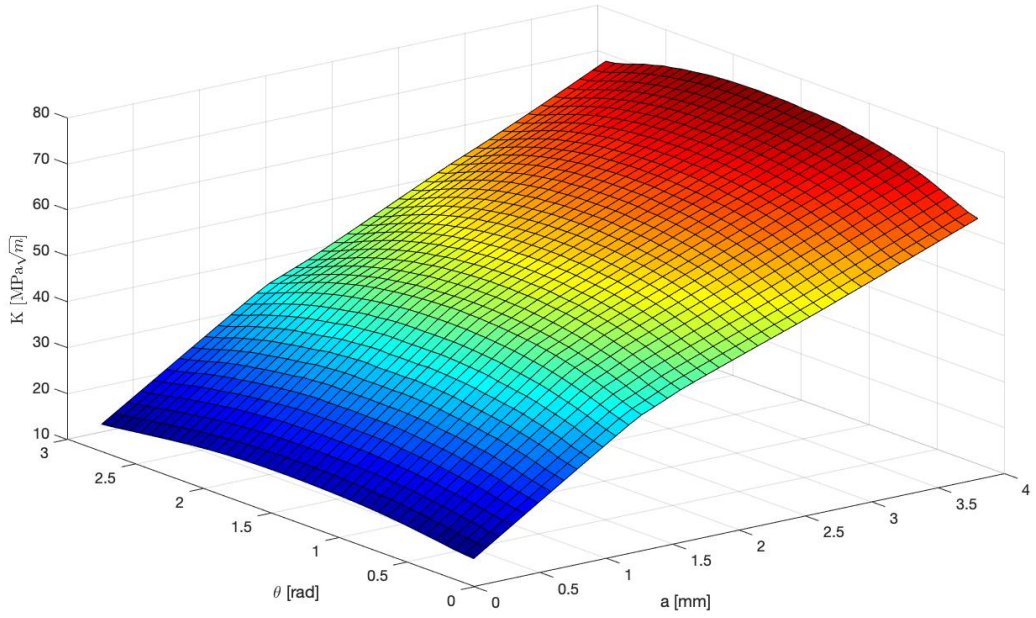

Figure 3.27: 3D Matlab plot of the variation of SIF along the front of the crack to $0.2mm \leq a \leq 4mm$ obtained in Ansys

As one would expect, the value of *K* grows as the size of the crack increases, in an almost linear manner. Additionally, we can see that the angle dependency does not affect the value of *K*, for small crack sizes. However, as a increases there is a clear asymmetry, where *K* assumes smaller values near the crack tip edges.

As mentioned at the beginning of the chapter, the modelling of crack propagation in FE aims to determine the expression of the geometric factor from the stress intensity factors for the geometry in question. Thus, similarly to the previous study, for each crack size, an average of the SIF along the crack vicinity was done. From the resulting K_I values the geometric factor was then calculated using the nominal stress that was previously mentioned of $33.7MPa$ since all the analysis used a loading situation of $n_z = 1$ was used in the analysis. The value of *Y* for the various crack sizes is then returned using Equation 3.10 previously used. These values are used to plot a 3D surface and a density plot, as a function of the parameters a and θ, using Matlab visualization toolbox.

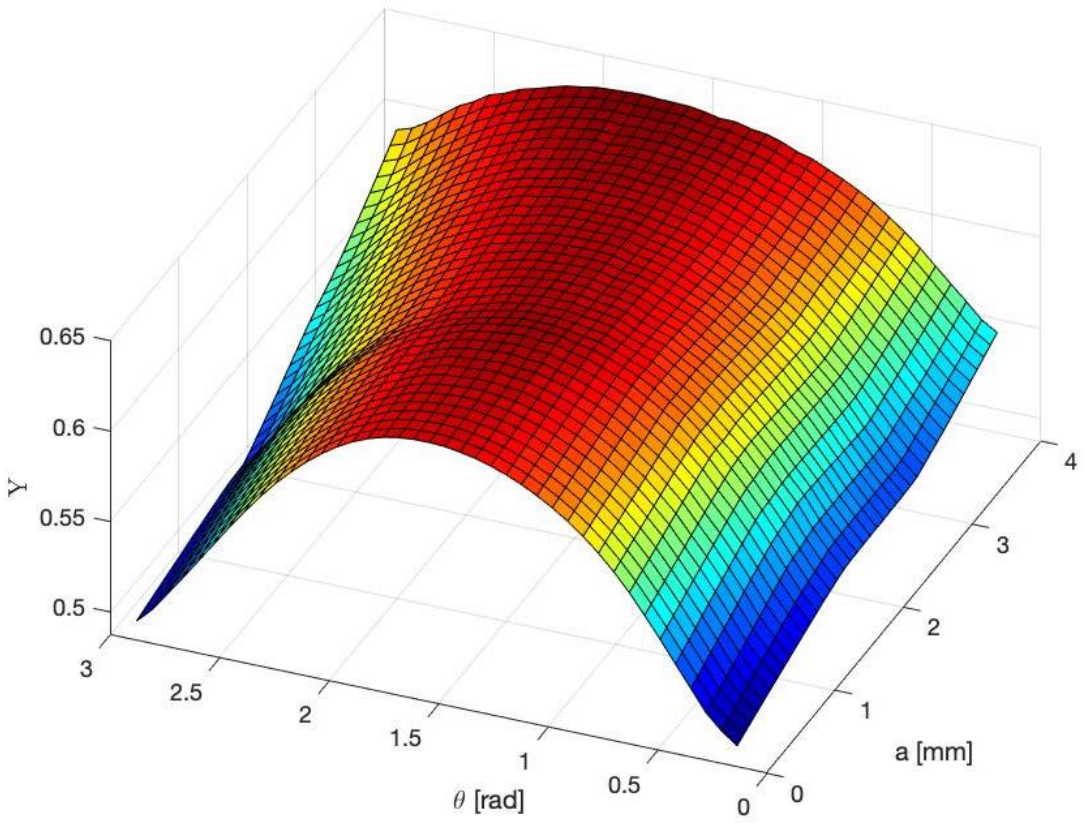

Figure 3.28: 3D Surface Plot - Geometric Factor

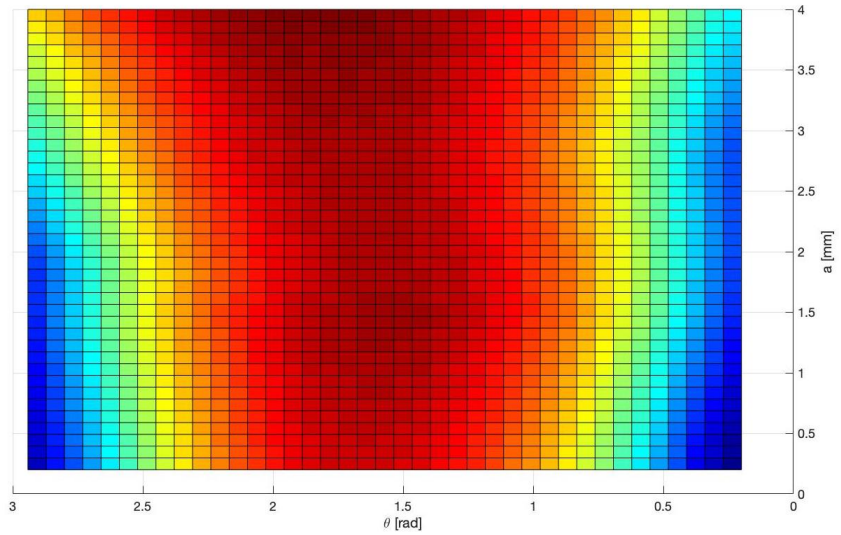

Figure 3.29: Density Plot - Geometric Factor

It is also observed that the peak of maximum stress as a increases tends to move away beyond 90° further from the rib, as explained above. This phenomenon can be better visualised in Figure 3.29.

Finally, it is possible to determine an expression for Y as a function of the parameters a and θ, by fitting a 5^{th} degree polynomial curve to a and 4^{th} degree polynomial curve to Θ. The expression obtained is the following:

$$
\begin{aligned}
Y(a,\Theta) = 0.3971 + 0.208a + 0.1693\Theta - 0.189a^2 - 0.09791a\Theta + 0.03483\Theta^2 + 0.07573a^3 + \\
0.06419a^2\Theta + 0.01082a\Theta^2 - 0.05099\Theta^3 - 0.01272a^4 - 0.02152a^3\Theta - \\
7.301 \times 10^{-5}a^2\Theta^2 - 0.002054a\Theta^3 + 0.008033\Theta^4 + 0.0007324a^5 + \\
0.002319a^4\Theta + 0.0001516a^3\Theta^2 + 5.828 \times 10^{-5}a^2\Theta^3 + 0.000325a\Theta^4
\end{aligned}
\tag{3.19}
$$

Since the geometry dealt is complex, it is expected that a polynomial fit would not match exactly the behaviour of the data. However, this result can be validated, since the obtained coefficient of determination is $R^2 = 0.982$, where the optimal value is near 1 and a value for the root mean squared error (RMSE) of 0.0049, with optimal value equal to zero.

Chapter 4

Implementation of Crack Propagation

In the previous chapter, an analysis was made on frame C2 in order to monitor the stress intensities felt and to get a picture of fatigue damage, across the component. A crack was inserted in the place of maximum stress where the value of the crack size was increased until an acceptable simulation was possible. The SIF values obtained for each crack size were then used to determine the geometric factor.

In this chapter, within the scope of Structural Integrity monitoring of the Epsilon TB-30 aircraft, the development of an automatic crack propagation prediction tool that simulates the crack propagation using real flight data of the aircraft under study is performed.

The tools used to developed this application were Python and the Streamlit package. This choice was made based on the fact that this package offers the ability to provide high quality applications, in an user-friendly way.

4.1 Crack-Propagator Application

4.1.1 Overview

The Crack-Propagator Web Application developed in this work has the purpose to enable any user to easily estimate and visualize the final crack size, allowing the user to configure several parameters that are fed to an iterative propagation model, like depicted in Figure 4.1.

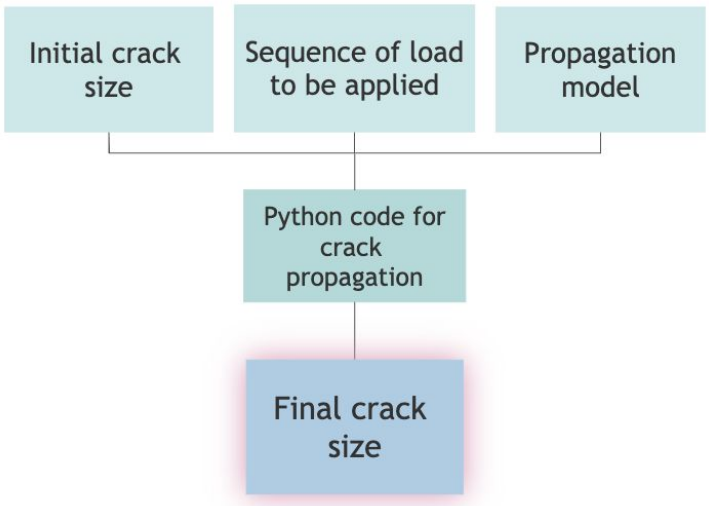

Figure 4.1: Algorithm block scheme

Below, a brief description of each input is provided:

- **Initial Crack Size** - numeric value in mm, ranging from [0,4]

- **Number of Dots** - corresponds to the number of nodes along the crack.
- **Load Sequence** - file containing flight data stored in a .csv file, with peak/valley sequences.
- **Propagation Model** - Available Models: [NASGRO, Walker]

Within the application, there is a Menu to select and configure these parameter options, in Figure 4.2 it is possible to see the user interface:

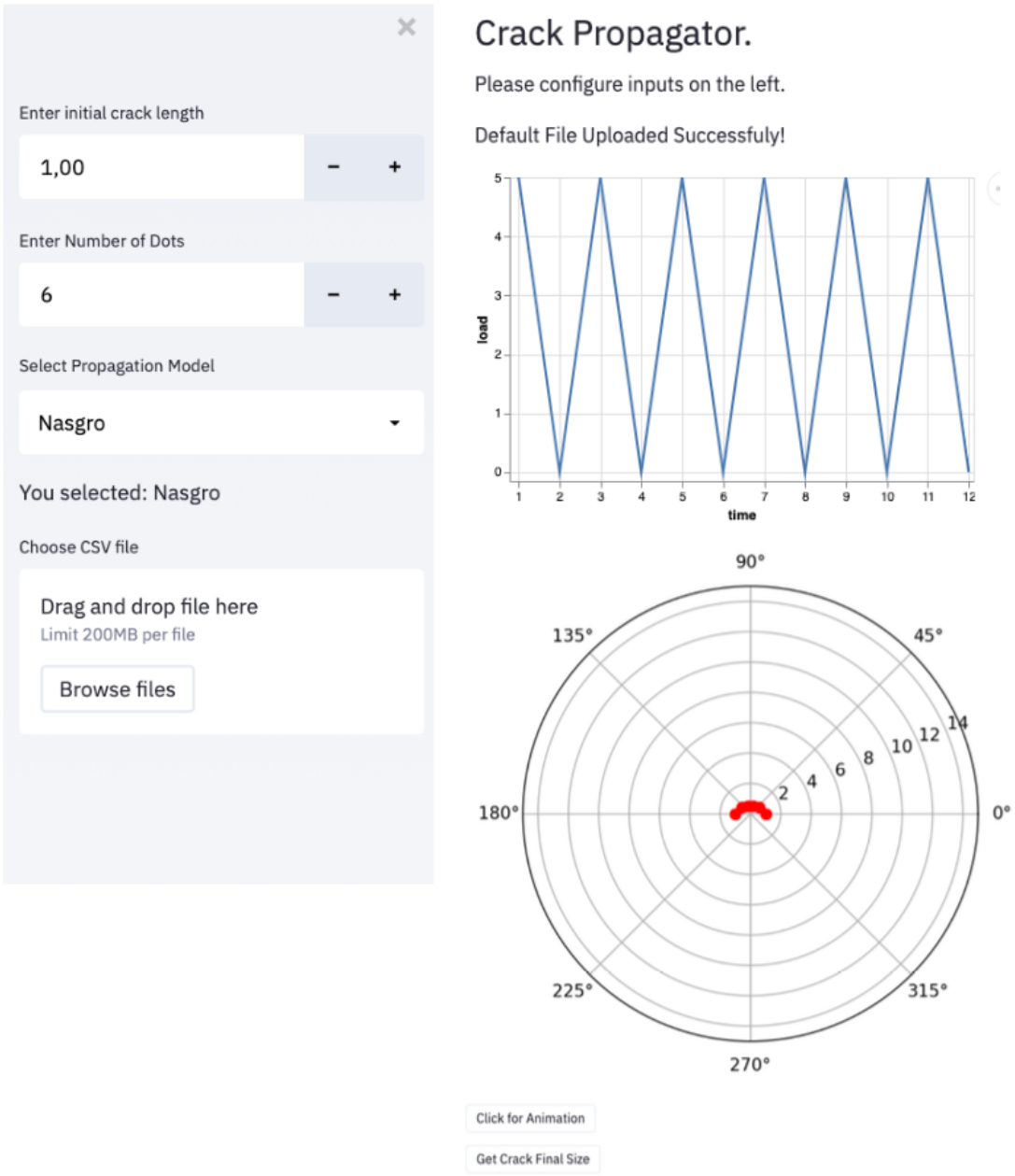

Figure 4.2: Application parameter configuration window

Once all the parameters are configured, by pressing the button ”Get Final Crack Size”, the crack starts to propagate, simulating a real-world scenario. This process terminates if the flight ends or if at least one of the stopping criteria is met. The following diagram in Figure 4.3 summarizes the steps of the crack propagation algorithm:

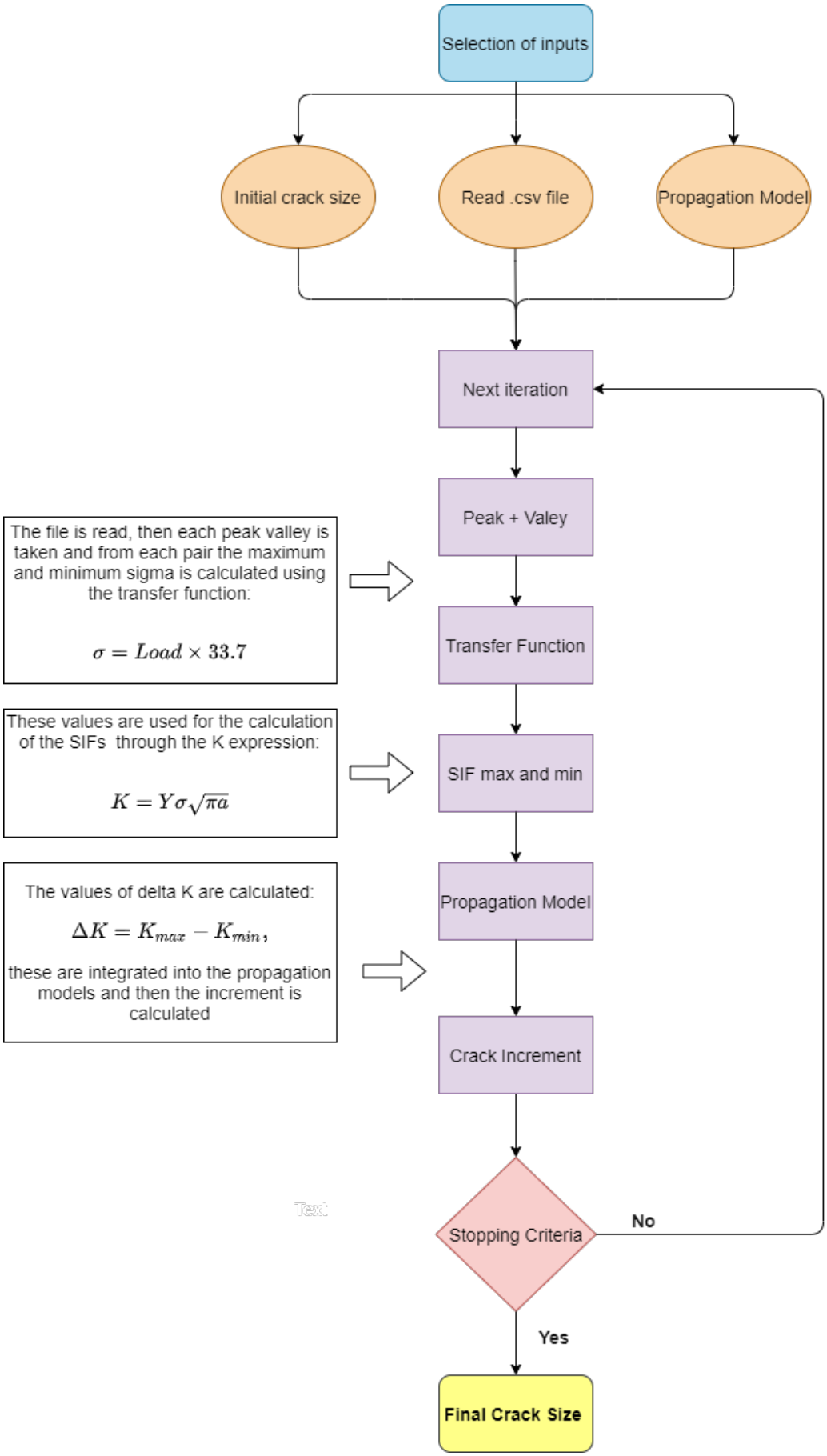

Figure 4.3: Crack Propagation Mechanism Diagram

For the next sections, a detailed description of the application functionality is provided for in-depth context of all the mechanism working behind the scenes.

4.1.2 Data Input

As seen previously, there are four types of inputs, but the focus will be on the flight data file. This file must obey a certain set of characteristics and formatting:

- Must be saved as a .csv file.
- Must contain only two columns: one representing elapsed time named 'time' in seconds and another representing the load factor suffered by the aircraft named 'load' expressed in G's.
- Each pair of rows should be in the form of "Valley-Peak", i.e. the first row of the file contains a smaller 'load' value than the second row and so on.

If all of these conditions are met, once the file is successfully uploaded, the flight spectrum is directly ploted on the screen. This enables the user to analyze and inspect the type of flight to be simulated.

4.1.3 Propagation

In order to determine the final size of the crack, a method based on an iterative process is implemented. To do so, it starts by defining the initial size of the crack and discretizing the number of points that define it. In the example of Figure 4.4 there are 5 points and an initial length a for a crack initially semi-elliptical.

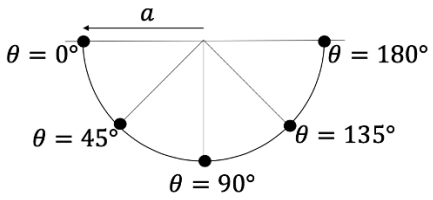

Figure 4.4: Initial crack

The crack propagation is an iterative process. At each iteration each of the points defining the crack front will "grow" in the radial direction. It was assumed that the points will move according to their initial orientation, that is, the point that is at 0 degrees will always move with that orientation as well as all the other points will have that behaviour, Figure 4.5. Thus, at each iteration an increment of the crack size (Δa) is calculated for each of the points.

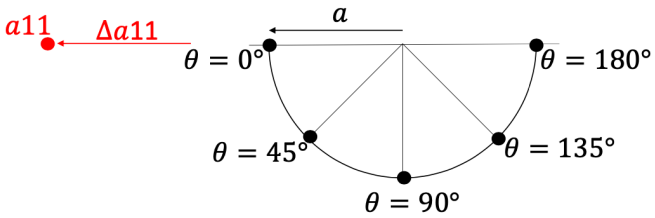

Figure 4.5: Increasing the crack length for a single point

At each iteration a crack size increment and a new crack length is calculated for each of the angular

positions, using the formula 4.1 below, where the next crack size is determined by incrementing the previous crack size, with selected propagation law. This procedure is repeated like shown in Figures 4.6 and 4.8, until the maximum stress is reached.

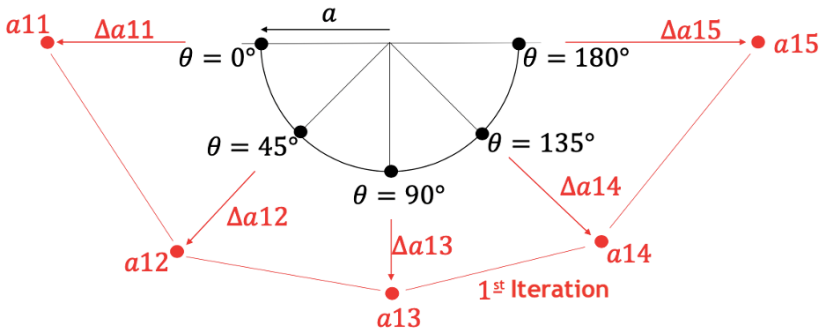

Figure 4.6: Increase of the crack length for all points

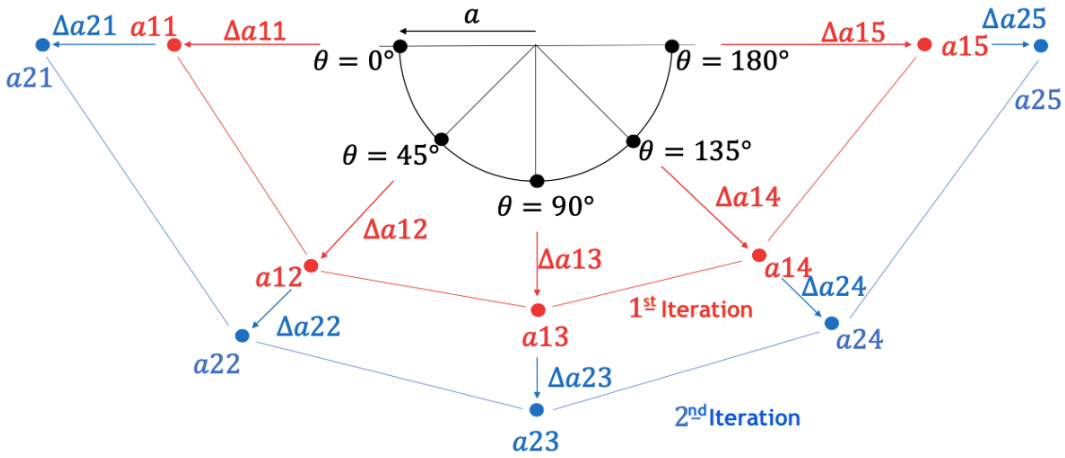

Figure 4.7: Second iteration- Crack Propagation

In a general form, we obtain for each crack size $a_{i,j}$:

$$a_{i+1,j} = a_{i,j} + \Delta a_{i,j} \qquad i \in [0, 1, .., n.], j \in [1, ..., n_{nodes}] \quad (4.1)$$

where i represents the iteration index and j the angular index and spans from 1 to the number of points in the crack n_{points}.

The increment is then calculated by choosing a propagation model. As seen previously in the inputs there are several propagation models that can be selected. Taking for example, the Paris law in Equation 4.2, we have:

$$\frac{da}{dn} = C(\Delta K)^n \implies a_{i+1,j} = C(\Delta K)^n + a_{i,j} \quad (4.2)$$

Then, the value of ΔK is calculated for each cycle by the value relative to the maximum and minimum, i.e. the peak and valley.

$$\Delta K = K_{max} - K_{min} \quad (4.3)$$

To calculate the value of *K*, the expression of the stress intensity factor is used with the geometric factor Y that we have deduced for our geometry and that depends on a and θ. This process is done individually for each of the points that define the front of the crack.

$$K_{max} = Y(a,\theta)\sigma_{max}\sqrt{\pi a} \quad (4.4)$$

$$K_{min} = Y(a,\theta)\sigma_{min}\sqrt{\pi a} \quad (4.5)$$

The geometric factor was obtained at the end of the previous chapter by fitting a polynomial curve to experimental data obtained in ANSYS. The σ values are calculated for each peak and valley of each cycle using data collected in flight, as described in the Expressions 4.6 and 4.7 where the values of the load are converted to stress when multiplied by a factor of 33.7. This value corresponds to the transfer function, relative to the critical location under study, which was obtained based on the PRODDIA AERO software from Stratosphere S.A. that was developed within the SHM TB-30 project, and the respective strain gauge installation on the aircraft [36]. The figure 4.8 shows the statistical distribution of the transfer function values in a box plot where the transfer function value used for the case corresponds to the median value.

$$\sigma_{max} = 33.7 n_{peak} \quad (4.6)$$

$$\sigma_{min} = 33.7 n_{valley} \quad (4.7)$$

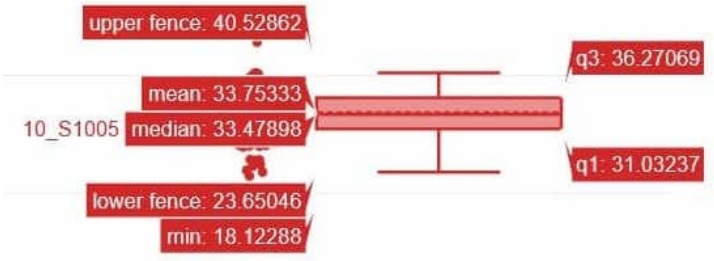

Figure 4.8: Scattered boxplot of Transfer function values sourced from PRODDIA AERO software derived from the aircraft instrumentation [36]

4.1.4 Parameters and Stopping Criteria

In this section, a summary of the parameters and validation domains of each propagation law is provided, along with stopping criteria, that happen when the crack reaches a certain size or a critical value of load is applied.

The definition of the crack propagation models are presented in Chapter 2. However, since Walker's law is nothing more and nothing less than an improvement of Paris Law by including the stress ratio, it was decided to proceed with the study only with the Walker and NASGRO models. Described by the Equations 2.30 and 2.31, respectively, these crack propagation models require, as verified in Chapter 2, parameters obtained through experimental tests, namely C_W , γ and n_W relative to equation 2.30 and p, q, C_N and n_N relative to Equation 2.31 .

Given the lack of such parameters for the case of the geometry under study, it was decided to select the parameters for an aluminum alloy 2024-T351 for Walker and NASGRO models. Regarding their source, propagation model parameters from the NASGRO® database of the document Fatigue Crack Growth Database for Damage Tolerance Analysis [37] were used and depicted in the Tables 4.1 and 4.2.

Table 4.1: Parameters for the Walker propagation model

Parameter	Values
Limit of no propagation ($\Delta K_{thR=0}$)	2.835 $MPa\sqrt{m}$
R limit values	$[-0.33; 0.74]$
C_W	1.1824 (m/cycle)/($\sqrt{m^{n_W}}/MPa^{n_W}$)
n_W	3.815
γ	0.691

Table 4.2: Parameters for the NASGRO propagation model

Parameter	Values
Limit of no propagation ($\Delta K_{thR=0}$)	0.879 $MPa\sqrt{m}$
R limit values	$[-0.3; 0.7]$
C_N	$7.23 \times 10^{-11} (m/cycle)/(\sqrt{m^{n_W}}/MPa^{n_W})$
n_N	3.6
p	0.5
q	1
Constraint factor α	2
Ratio S_{max}/σ_0	0.3

Finally, the stopping criterion for crack propagation is established. It was decided to establish that the crack propagation ends when the fracture toughness value K_C, presented in Table 3.2, which corresponds to the component failure, is reached. In case the referred value is not reached, the crack propagation ends when its dimension reaches a depth of $4mm$.

4.2 Flight Regimes

The need for flight regime recognition is crucial in aircraft maintenance and continuing airworthiness. Having information about the events to which the aircraft has been subjected during its service life is of great help for maintenance actions, failure prevention and life extension. The Epsilon TB-30 fleet is used by the Portuguese Air Force for instruction purposes encompassing all instruction modules of a pilot course which are:

1. Contact = aerobatics + circuits
2. Formation flight
3. Navigation
4. Instruments
5. Maintenance

Part of the severe regime of this aircraft involves aerobatic flights, which is a specialized form of flight, where the aircraft's performance and attitudes change rapidly. The flight profile is beyond normal operations and may involve rolls, loops and stalls. Such regimes are especially demanding for aircraft structures and should enter into special consideration when monitoring flight loads on aircraft that perform them on a regular basis. Although airframes are designed to withstand g-forces (both positive and negative) experienced during aerobatic maneuvers, g limitations are established to ensure that the aircraft structure is able to withstand the maximum specified loading. The cumulative effect of deliberately imposing maximum or greater loads on numerous occasions can have an adverse effect on the fatigue life of the aircraft by weakening the aircraft structure.

In Figure 4.9 2 examples of flight data corresponding to flights in severe regime, performed by this aircraft are shown. It is possible to observe that high load peaks are reached numerous times during the spectra, which is a strong indicator of aerobatics or abrupt maneuvers.

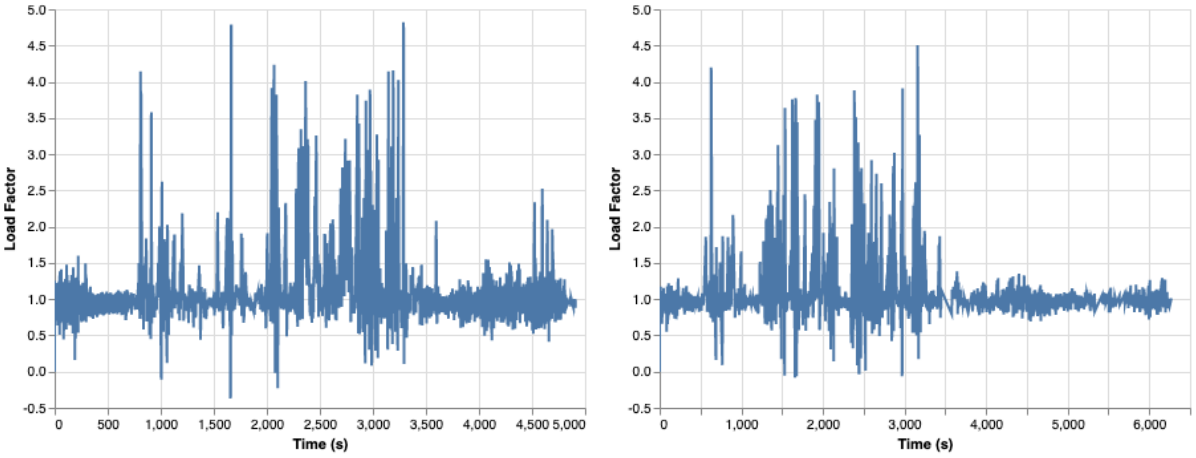

Figure 4.9: Aerobatic flight spectra

In contrast, in Figure 4.10 two examples of flight data for a less severe regime are shown. In these spectra it is possible to observe a greater stability in the amplitude of the flight cycles keeping at lower load factor values ending up never surpassing a value of 1.7.

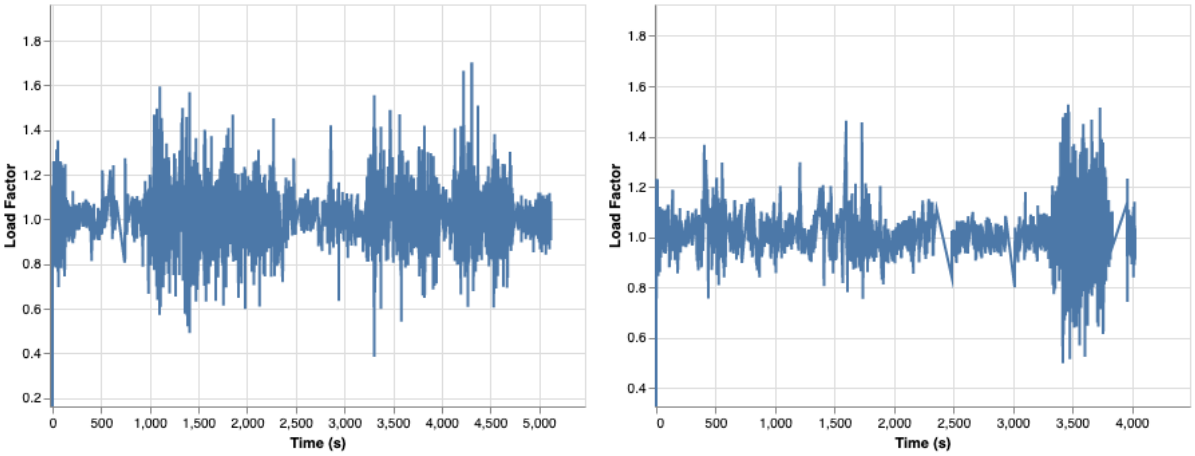

Figure 4.10: Instrument flight spectra

There is an upward graduation in the load factor with increasing severity of manoeuvre. In normal operations, non-severe types of flight, the required load factor (and consequently the weight of the aircraft) is lower than if the aircraft is used in training or aerobatic manoeuvres, as these result in higher manoeuvre loads.

4.3 Results and Analysis

In this section several experiments were performed consisting in varying a set of inputs namely initial crack size, propagation model and flight severity regime. Through these approaches it is intended to compare the behavior of the crack growth, more specifically the crack growth rate. For analysis purposes it was considered relevant to select 8 simulations with the following parameter configuration shown in Table 4.3.

Table 4.3: Crack propagation experiments parameters

Simulation Nº	Propagation Model	Type of Flight	Initial Crack size (mm)
1	Walker	Severe	1
2	NASGRO	Severe	1
3	Walker	Non-Severe	1
4	NASGRO	Non-severe	1
5	Walker	Severe	2
6	NASGRO	Severe	2
7	Walker	Non-Severe	2
8	NASGRO	Non-Severe	2

Regarding the flight data used in these experiments it should be noted that these are only samples of real flights corresponding mostly between 45 minutes and 1 hour and 30 minutes of flight. For simulation purposes and since these times are notoriously short to verify a significant increase in crack size, the same file was repeated n times in order to multiply the number of flight cycles. Additionally, in order to mitigate the limitation inherent to the lack of diversity of the flight under study, it was decided to agglomerate different samples, related to the same type of flight resulting in a file with more information in an attempt to cover different scenarios encountered in the operation of this aircraft.

4.3.1 Experiments

4.3.1.1 Part 1 - Comparing Propagation Models

This first part of the section shows the results corresponding to the first 4 simulations described above, with the respective initial conditions. Firstly, the effect that each propagation model causes on the crack size growth was studied, for the same flight regime. Below, the graphs that demonstrate this behaviour for a non-severe and severe flight as a function of the number of cycles respectively in Figure 4.11 and Figure 4.12 are represented. On both plots,the red line corresponds to Nasgro and the blue line to Walker law, the initial crack size was set to $1mm$ and on the y axis the crack depth, which corresponds to crack node $\theta = \frac{\pi}{2}$, is represented in mm.

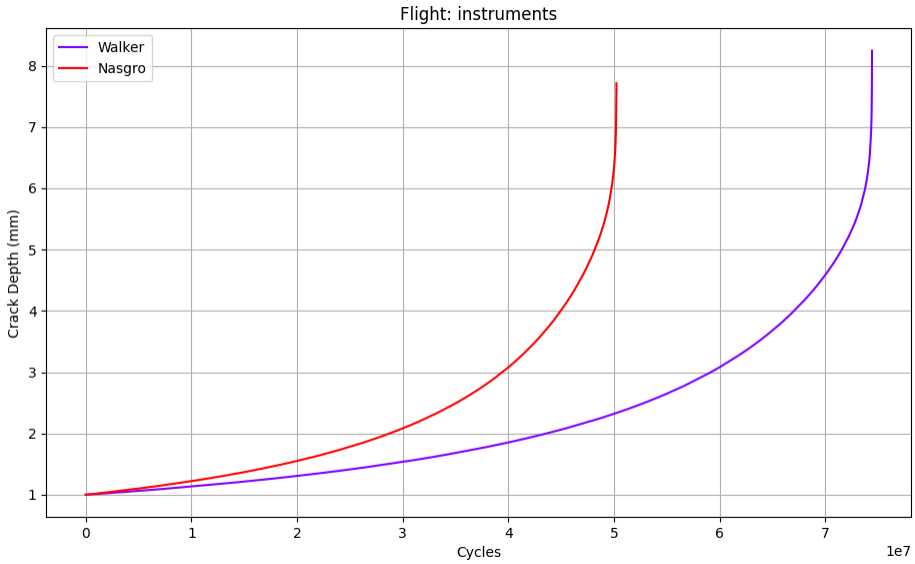

Figure 4.11: Nasgro (Red) vs Walker (Blue) comparison of crack depth growth for non-severe flight

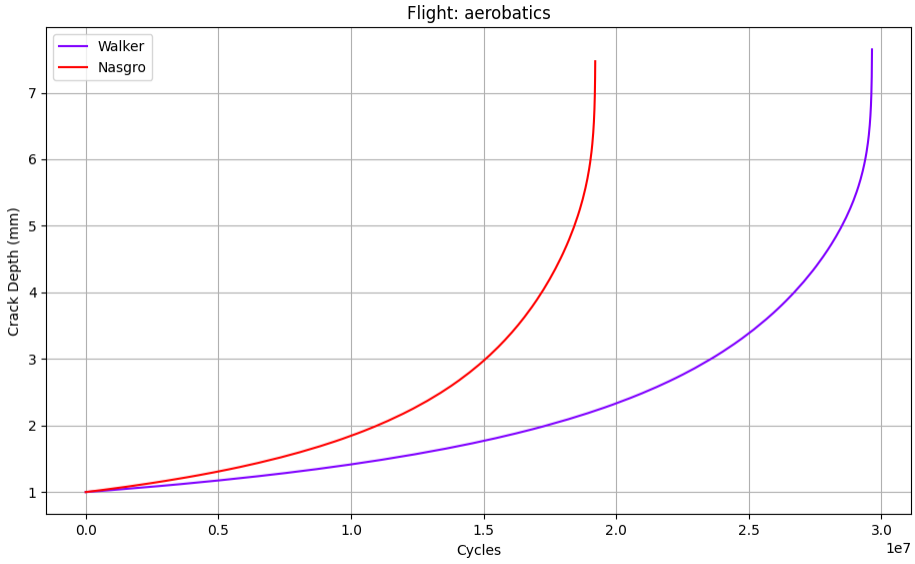

Figure 4.12: Nasgro (Red) vs Walker (Blue) comparison of crack depth growth for severe flight

Analysing the two graphs above, there is an evident difference on the number of cycles to reach the same crack size. In both cases, a steeper growth is observed earlier for the NASGRO model than for the Walker model, with a deviation from the maximum of approximately 33%. Therefore, as expected, it is noticed that the NASGRO model always presents a faster crack propagation than Walker's model. The deviation obtained can be explained by the fact that the NASGRO model contemplates not only the average stress effect described by the ratio R, but also the initial and final propagation regions which, by presenting the asymptotic behavior of Figures 4.11 and 4.12, are responsible for an acceleration of the crack propagation. By considering the initial and final stages of propagation, a more realistic and more conservative behavior from the point of view of crack growth prediction is obtained.

4.3.1.2 Part 2 - Comparing flight regimes

For the next two experiments a study on the influence of different flight regimes on the growth of the crack was performed. Figures 4.13 and 4.14 compare the crack growth curves for 2 flight regimes of opposite severity, when governed by the same propagation model.

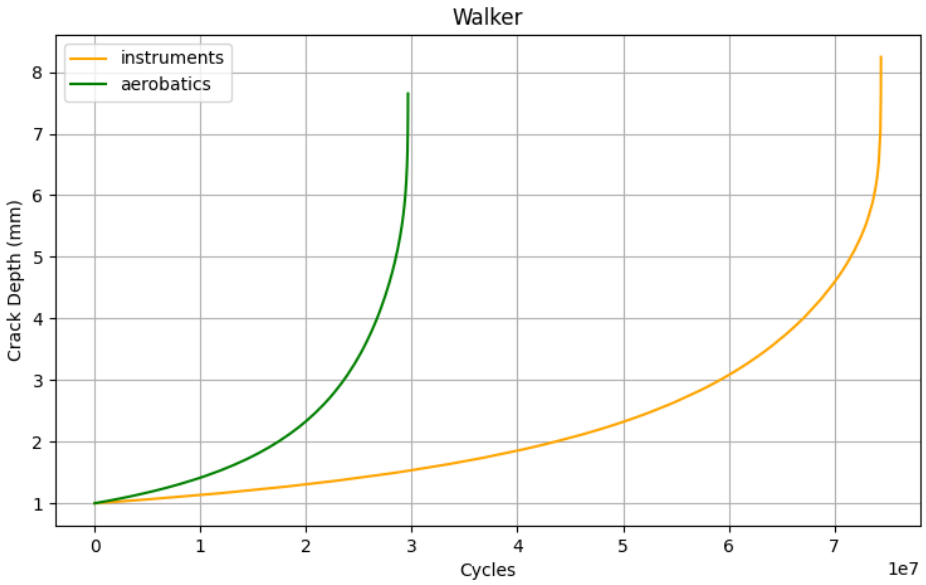

Figure 4.13: Severe (Green) vs. non-severe (Orange) comparison of crack depth growth for Walker model

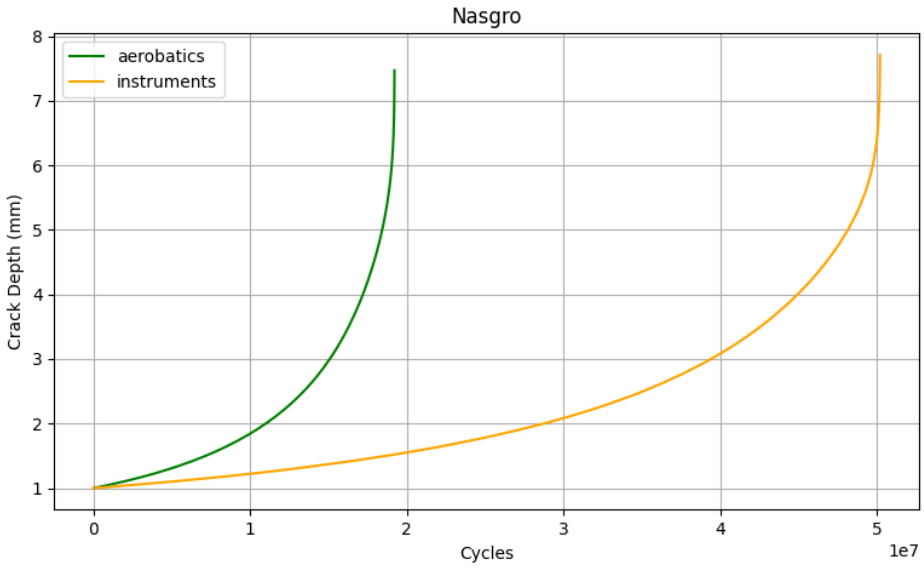

Figure 4.14: Severe (Green) vs. non-severe (Orange) comparison of crack depth growth for Nasgro model

As expected, the crack growth rate is prominently higher for the more severe flight regime presenting a deviation of approximately 60 %. This translates into the need to apply 2.5 times more cycles to the non-severe flight to exhibit the same trend as in severe flight. This discrepancy in crack growth rate is due to the drastic difference in load factor experienced in the two different flight regimes, as demonstrated in the previous section in Figures 4.9 and 4.10.

It is important to mention that to obtain these results, the limits of no propagation showed in Tables 4.1 and 4.2 were omitted. After several simulations, for an initial crack size of $1mm$, it was observed that even for a flight in severe regime, ΔK values higher than the non propagation limit were rarely obtained, preventing the crack increment and consequently the crack growth. With this in mind and since is intended to study and compare the severity between missions, it was decided to consider, for this initial crack size, that the crack would always propagate, regardless of the value of ΔK.

4.3.1.3 Part 3 - Comparing Initial Crack Sizes

For the third part of the study, it was considered relevant to study the influence that the initial size of the crack has on its propagation speed. To this end, it was established that the initial crack size would be set to $2mm$ and the experiments of Part 1 and 2 were repeated for the new initial crack size. In the first two Figures it is possible to see the comparison of the crack growth behavior for non-severe 4.17 and severe 4.18 flight regime, for the two propagation models for two different initial crack sizes. Dashed lines and full lines represent, respectively, initial crack size equal to $1mm$ and $2mm$.

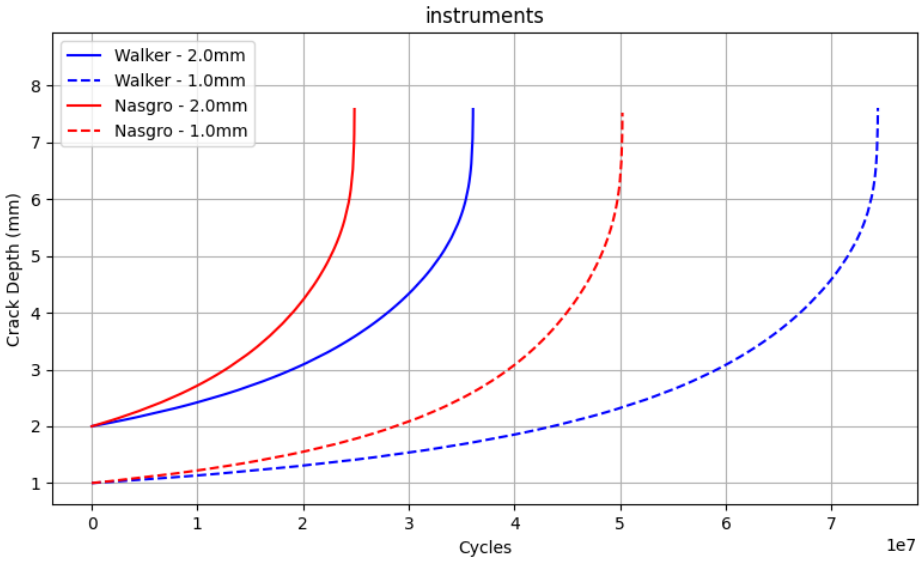

Figure 4.15: Initial Crack size (full vs dash lines) and Propagation Law (Red vs Blue lines) comparison of crack depth growth for non-severe flight

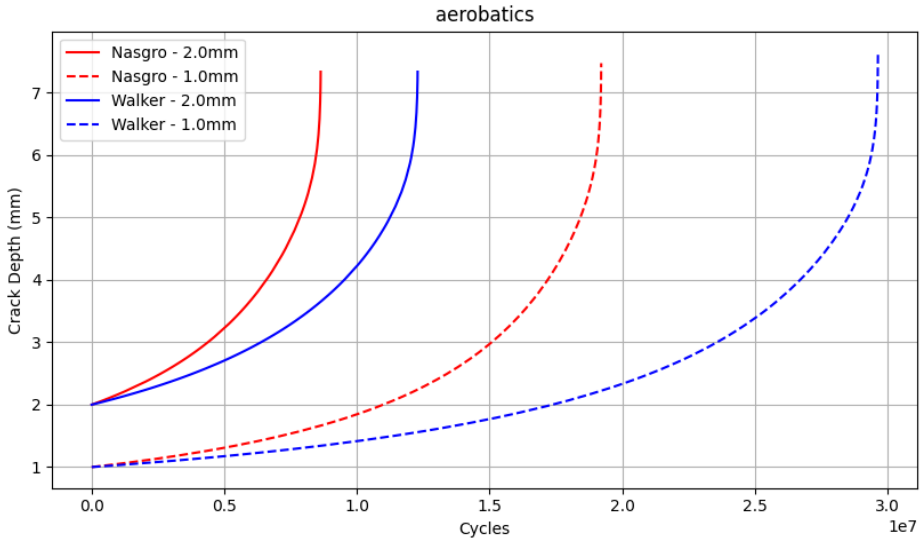

Figure 4.16: Initial Crack size (full vs dash lines) and Propagation Law (Red vs Blue lines)comparison of crack depth growth for severe flight

Through the first two graphs represented above, it is possible to observe the expected behaviour in the difference in the growth of the curves for the Walker and NASGRO model for $a = 2mm$, being the deviation between the two models for the two initial crack sizes of approximately 30%. Then, in Figures 4.17 and 4.18 an insight into the crack growth rate by comparison for the two flight regimes for two initial crack sizes is given.

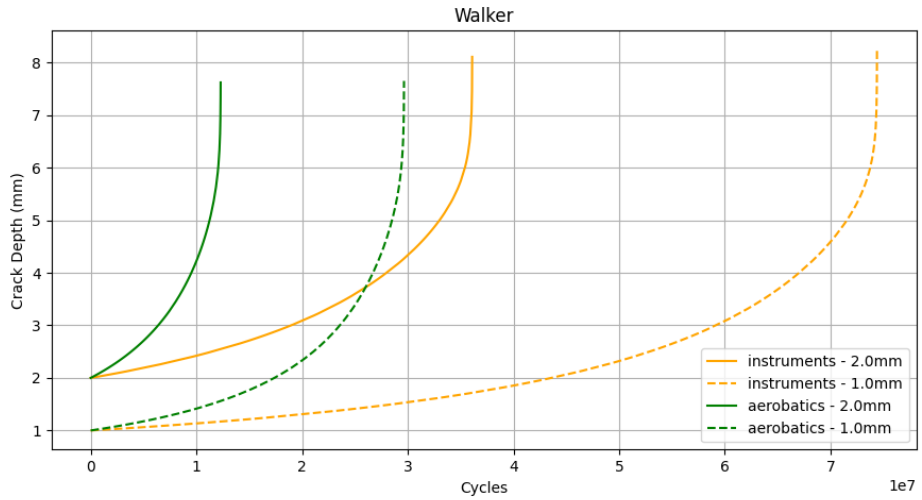

Figure 4.17: Initial Crack size (full vs dash lines) and Flight regime (green vs orange) comparison of crack depth growth for Walker model

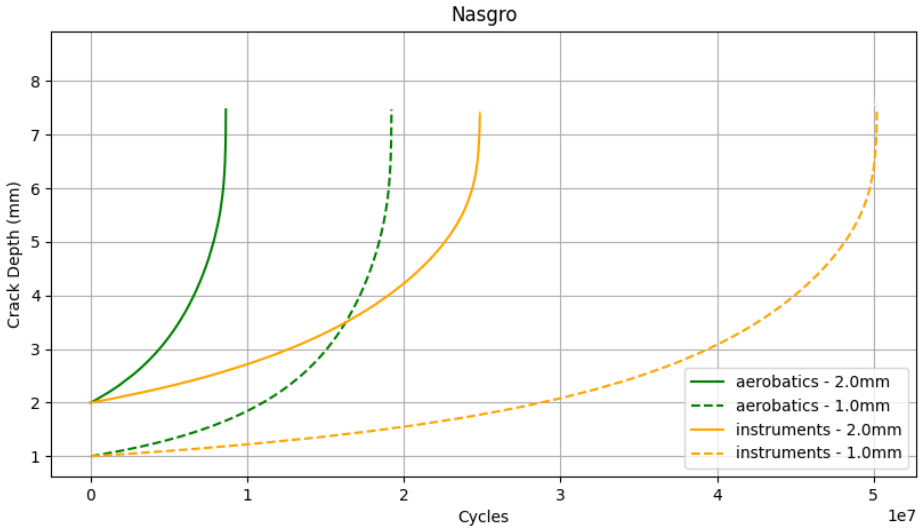

Figure 4.18: Initial Crack size (full vs dash lines) and Flight regime (green vs orange) comparison of crack depth growth for Nasgro model

Regarding both graphs, there is a relative deviation between curves that correspond to an initial crack size of $2mm$ of approximately 80% and for crack size $1mm$ it is 60.6%. It is also possible to observe that, despite a smaller initial crack size, a severe flight reaches asymptotic behaviour faster than a non-severe flight with a larger initial crack size, for both propagation laws.

In this part 3 of the experiments, the non-propagation limit was imposed since it allowed the crack to increase and grow. This is explained by the fact that the crack depth a is proportional to K which consequently implies a greater ΔK, surpassing more easily the non-propagation limit.

Chapter 5

Final Remarks

In this chapter, the conclusions of the present study are presented and recommendations are made for possible future studies within the scope of structural monitoring in concrete in the propagation of fractures due to fatigue of the Epsilon TB-30 fleet.

5.1 Conclusions

5.1.1 Finite Element Method and Modeling

Regarding the modeling of the crack in FE, using ANSYS, it is concluded that it is possible to establish an automatic crack propagation methodology through an interaction between ANSYS and MATLAB program. It is also concluded that it is possible to determine stress intensity factors automatically for any geometry with a semi-elliptical crack, since the results obtained from ANSYS show a small error when compared to theoretical values from Newman's model. Indeed it is possible to conclude that, despite the complexity of the geometry under study and the difficulty of recreating the real conditions to which the airframe is subjected, together with the time and computational resources required for each simulation, the results obtained with ANSYS are quite satisfactory.

For the case under study, it is concluded that the geometric factor Y is well characterized by a fifth order function of a and a fourth order function of Θ. Despite the difficulties encountered in modeling the crack, due to the complexity of the geometry of the structure where it was inserted, it is possible to obtain good results with ANSYS in three-dimensional Fracture Mechanics problems.

Regarding the parameters of the propagation laws, the nonexistence of crack propagation parameters for the studied structure induced the use of parameters relative to a 2024-T351 aluminum alloy. The fact that these parameters were not appropriate to the geometry of the structure under study, influenced the crack propagation results and, consequently, the percentage difference in the severity comparison, representing a limitation of this study.

5.1.2 Crack Propagation

There are 2 operating regimes that are used in the operation of the Portuguese Air Force Epsilon TB-30 aircraft that are used for instruction. Due to this amplitude in the severity of flight regimes it is essential to monitor and predict the behavior of existing cracks in critical structures of the aircraft, specifically in the frame that supports the two wing spars. In this sense, for this work an application was developed with a crack propagation model that is specific for this critical area, where the user can simulate for a given flight, regardless of the mission type, the propagation of a crack, customizing a set of relevant parameters - like propagation law, initial crack size and number of repetitions of a flight file. From this tool, it was possible to perform the simulations that were the target of study in this work.

Through the results obtained it is concluded that, as expected, the growth of a crack for a severe regime is notably more accelerated. For the case in which the initial crack size is $1mm$, a relative deviation of 60%

is observed between the different severity regimes, for both propagation models, i.e. in the case of severe flight the crack takes 60% less cycles to reach the critical value. It is also concluded that the initial size of a crack has a high influence on the growth rate. Comparing the deviation for 2 different initial crack size, $1mm$ and $2mm$ it was observed that the crack needs 55% and 63% less cycles to reach the crack's limit respectively for the severe regime and the non-severe regime, for a crack with larger initial size.

5.2 Future Work

Due to constraints and limitations, there are several ways of extending and improving this study, in order to have a more complete model that returns more realistic and broad results.

The fact that the geometric parameter Y is only valid for a crack when it reaches the value of 4mm implies that this parameter is no longer valid for larger crack sizes, it would then be necessary to extend the domain of validity of this parameter, performing additional simulations in Ansys, or in other identical software, in order to contemplate larger crack sizes.

Regarding the study of automatic crack propagation it would be advantageous to quantify the uncertainty of the flight data, so that a confidence interval can be provided for the number of cycles required to reach a given crack size.

A future, and within possibilities, instrumentation of more aircraft of the Epsilon fleet with an extensions (deformations) and accelerations (load factors) collection system would lead to a wider monitoring scope, by allowing the assessment of the fatigue index to which they are subjected throughout their operation. By taking into account data collected from different aircraft, belonging to the same fleet, it is possible to make a more complete and reliable study of fatigue crack propagation. Therefore leading to the possibility of establishing more accurately the inspection intervals of these aircraft.

It would also be advantageous to perform this same study for other critical locations of the aircraft and even extend it to different aircraft fleets of the Portuguese Air Force whose operation covers different severity regimes.

References

[1] "AEROSPATIALE EPSILON TB-30." https://www.emfa.pt/aeronave-9-aerospatiale-epsilon-tb30. Accessed: 2020-05-09.

[2] CEAT, *Epsilon - documents de synthese suite a la campagne d'essai de fatigue. Technical report, SOCATA, Groupe Aeroespatiale*. SOCATA, Groupe Aeroespatiale, 1996.

[3] M. Milharadas, *Relatório do Tirocínio ENGAER. Academia da Força Aérea Portuguesa*. 2004.

[4] J.Silva, *Relatório do Tirocínio ENGAER. Academia da Força Aérea Portuguesa*. 2003.

[5] B. Serrano, "Previsão do tempo de vida de fadiga da aeronave epsilon tb-30 da fap(grau de mestre. instituto superior técnico, academia da força aérea," master thesis, Instituto Superior Técnico, sep 2009.

[6] P.Gameiro, "Desenvolvimento e implementação de uma metodologia de seguimento de vida de fadiga da aeronave epsilon tb 30 da força aérea portuguesa (grau de mestre). instituto superior técnico, academia da força aérea.," Master's thesis, 2016.

[7] T. Martins, "Mechanical study of an aircraft's structural condition," master thesis, Instituto Superior Técnico, jun 2019.

[8] T. de Oliveira Barros, "Previsão do tempo de vida de fadiga da aeronave epsilon tb-30 baseada em ensaios experimentais representativos da operação da aeronave em provetes que simulam as zonas críticas," master thesis, Academia da Força Aérea, Sintra, dec 2019.

[9] S. Suresh, *Fatigue of Materials*. Cambridge University Press, 1998.

[10] T. Anderson and T. Anderson, *Fracture Mechanics: Fundamentals and Applications, Third Edition*. Taylor & Francis, 2005.

[11] W. Schutz, "A history of fatigue," *Engineering Fracture Mechanics*, vol. 54, no. 2, pp. 263 – 300, 1996.

[12] D. Broek, *Elementary engineering fracture mechanics*. Springer Netherlands, 1982.

[13] S. D. Antolovich, A. Saxena, and W. W. Gerberich, "Fracture mechanics - an interpretive technical history," *Mechanics Research Communications*, vol. 91, pp. 46–86, 2018.

[14] Y. Lee, J. Pan, R. Hathaway, and M. Barkey, *Fatigue Testing and Analysis: Theory and Practice*. Elsevier Science, 2011.

[15] C. de Moura Branco, *Mecânica dos materiais: teoria e aplicações*. MCGRAW-HILL INTERAME, 2012.

[16] A, "Fases fadiga." https://www.ques10.com/p/21915/explain-the-mechanism-of-fatigue-failure/, 2020. Accessed: 2020-04-05.

[17] B. Farahmand, G. Bockrath, and J. Glassco, *Fatigue and Fracture Mechanics of High Risk Parts: Application of LEFM & FMDM Theory*. Springer US, 2012.

[18] L. Pook, "The linear elastic analysis of cracked bodies, crack paths and some practical crack path examples," *Engineering Fracture Mechanics*, vol. 167, pp. 2–19, 2016. SI:CRACK PATHS 2015.

[19] N. Dowling, *Mechanical Behavior of Materials: Engineering Methods for Deformation, Fracture, and Fatigue*. Pearson Prentice Hall, 2007.

[20] A. manual, "Fracture toughness as a function of thickness," 2019. [Online; accessed April 17, 2020].

[21] C. Sun and Z. Jin, *Fracture Mechanics*. Elsevier Science, 2011.

[22] P. R. Strohaecker, "Mecanica da fratura," 2019. [Online; accessed April 17, 2020].

[23] E. Hackett, K. Schwalbe, R. Dodds, A. C. E.-. on Fracture Testing, and E. S. I. Society, *Constraint Effects in Fracture*. No. v. 1 in ASTM STP 1171, ASTM, 1993.

[24] W. Brocks, "Numerical aspects of the path-dependence of the j-integration in incremental plasticity," 2019. [Online; accessed April 20, 2020].

[25] J. Schijve, *Fatigue of Structures and Materials*. Springer Netherlands, 2008.

[26] Mechanicalc, "crack growth," 2014. [Online; accessed April 28, 2020].

[27] S. Mettu, V. Shivakumar, J. Beek, F. Yeh, L. Williams, R. Forman, J. McMahon, and I. Newman, "Nasgro 3.0: A software for analyzing aging aircraft," 02 1999.

[28] M. Kuna, *Finite Elements in Fracture Mechanics: Theory - Numerics - Applications*. Solid Mechanics and Its Applications, Springer Netherlands, 2013.

[29] I. Raju and J. Newman, "Stress-intensity factors for a wide range of semi-elliptical surface cracks in finite-thickness plates," *Engineering Fracture Mechanics*, vol. 11, no. 4, pp. 817 – 829, 1979.

[30] I. Newman and I. Raju, "Stress intensity factor equations for cracks in three-dimensional finite bodies subjected to tension and bending loads," *NASA Technical Memorandum*, vol. 85, 05 1984.

[31] "Matweb - the online materials information resource. (2020)." http://www.matweb.com. Accessed: 2020-08-17.

[32] E. Wang, T. Nelson, and R. Rauch, "Back to elements - tetrahedra vs. hexahedra," 01 2004.

[33] S. Teh, A. Andriyana, S. Ramesh, I. Putra, P. Kadarno, and J. Purbolaksono, "Tetrahedral meshing for a slanted semi-elliptical surface crack at a solid cylinder," *Engineering Fracture Mechanics*, p. 107400, 11 2020.

[34] S. Strobl, P. Supancic, T. Lube, and R. Danzer, "Surface crack in tension or in bending – a reassessment of the newman and raju formula in respect to fracture toughness measurements in brittle materials," *Journal of the European Ceramic Society*, vol. 32, p. 1491–1501, 07 2012.

[35] EADS, *Epsilon Aircraft crew operating manual*. 1983.

[36] "Shmtb30." `http://tb30.stratosphere-technologies.com/index.html`. Accessed: 2021-02-09.

[37] "Federal aviation administration. fatigue crack growth database for damage tolerance analysis. (2005). va: National technical information service." http://www.tc.faa.gov/its/worldpac/techrpt/ar05-15.pdf. Accessed: 2020-12-19.